Hollow Disk Electromechanical Coupling Cx/Co Boosting

Yafei Li
Clark Nguyen

Electrical Engineering and Computer Sciences
University of California at Berkeley

Hollow Disk Electromechanical Coupling Cx/Co Boosting

by Yafei Li

Research Project

Submitted to the Department of Electrical Engineering and Computer Sciences, University of California at Berkeley, in partial satisfaction of the requirements for the degree of **Master of Science, Plan II**.

Approval for the Report and Comprehensive Examination:

Committee:

Professor Clark Nguyen
Research Advisor

(Date)

* * * * * * *

Professor Kristofer Pister
Second Reader

(Date)

Hollow Disk Electromechanical Coupling C_x/C_o Boosting

By Yafei Li

Committee:

Professor Clark Nguyen, Research Advisor

Professor Kristofer Pister, Second Reader

ABSTRACT

The growing need for high performance but low power microelectromechanical system (MEMS) devices capable of operating at various frequency regimes, including high frequency (HF), very high frequency (VHF) and ultra-high frequency (UHF), fuels an increasing demand for resonators with simultaneous high quality factor (Q) and high electromechanical coupling, as gauged by the motional-to-static capacitive ratio (C_x/C_o). Capacitive-gap transduced resonators have already posted some of the highest disk C_x/C_o-Q products to date at HF and low-VHF. Attaining similar performance at the high-VHF and UHF ranges, however, if more difficult, as it requires electrode-to-resonator gaps considerably smaller than previously demonstrated.

This thesis explores a method that raises C_x/C_o without excessive gap-scaling by hollowing out a disk resonator structure, which reduces the dynamic mass and stiffness of the structure. Since C_x/C_o goes as the reciprocal of mass and stiffness, a hollow disk can have considerably stronger electromechanical coupling than a solid one at the same frequency. This work introduces two types of hollow disks: asymmetric and symmetric.

In an asymmetric hollow disk, a thin sidewall ring protrudes upward from the edges of an inner disk that itself anchors to the substrate via a center stem. The inner disk still vibrates in the radial contour mode in the radial direction. However, a few nonidealities influence this asymmetric structure, including transverse vibration of the inner disk and reduction of the nominal resonance frequency. The sidewall vibrates in a radial cantilever mode, which boosts C_x/C_o even higher. In addition, the negative capacitance ($-C_e$) in the equivalent circuit does not always equal the static capacitance (C_o). As a result, an 80 MHz asymmetric radial contour hollow disk achieves $C_x/C_o = 0.142\%$ and $C_x/C_e = 0.358\%$ with a 148 nm electrode-to-resonator gap and a 20 V DC bias, while a solid disk only has $C_x/C_o = 0.015\%$ with the same resonance frequency, gap spacing, and DC bias.

In a symmetric hollow disk, the sidewall ring protrudes in both upwards and downwards directions along the inner disk edges. As long as the stem anchor is small, the symmetry eliminates vertical vibration nonidealities, allowing for even better performance. Unfortunately, post-fabrication stress gradients rendered testable only a large-stemmed 98 MHz symmetric hollow disk. Although its large stem compromised its mode shape, this device still achieves $C_x/C_o = 0.261\%$ and $C_x/C_e = 0.430\%$ with a 50 nm electrode-to-resonator gap and a 7 V DC bias, both higher than achievable by a similar frequency solid disk. C_e is only $0.442C_o$, which makes its parallel frequency (f_p) is parabolically dependent on DC bias.

TABLE OF CONTENTS

ACKNOWLEDGMENTS

I am indebted to Professor Clark Nguyen for his generous support and guidance. He transferred me from mechanical engineering to electrical engineering and granted me research funding even at the very beginning. For the past three years, he brought a lot of exciting projects and funding to the group and gave me lots of freedom to explore what I want to do. Undoubtedly, he supported and guided me along the journey. Even at the end, he unconditionally agreed to write a recommendation letter for me applying the master of architecture program.

I would like to thank Professor Kristofer Pister for serving on the second reader of this thesis and teaching me the best circuit course I have ever learned at UC Berkeley, Professor Liwei Lin for bringing me into the fascinating world of MEMS and Professor Philip Marcus for admitting me to mechanical engineering at UC Berkeley.

I thank the Berkeley Nanolab staff for continuously doing their best to upkeep the lab and all Nanolab members for helping me and creating such a friendly laboratory.

I am proud to be a BSAC member, and I thank the BSAC staff for arranging lots of great seminars and semi-annual IAB meetings. I enjoyed discussing interesting questions with other researchers and industrial members and kept my thought closer to the industrial frontier.

I am grateful to my group members Ruonan Liu, Jalal Nilchi, Alper Ozgurluk, Kieran Peleaux, Qianyi Xie, Gleb Melnikov, Alain Anton, Thanh-Phong Nguyen, Kyle Tanghe. Especially to Ruonan Liu, she helped, supported, and guided me a lot in the lab. To Kieran Peleaux, he offered generous help along the application of the architecture program.

I also would like to thank Shirley Salanio for her endless support as a graduate advisor.

I am in great debt to Professor Anthony Dubovsky, who was my instructor of VS280 in the department of architecture in these last two semesters. He has become my mentor for the rest of my life journey. Without his generous mentorship, I would not be able to get the offer from architecture at UC Berkeley. I am looking forward to studying in Wurster Hall.

I also would like to thank a few VS280 classmates, Qing Tian, Robin Chandler and Xin Yu. With their continuous encouragement, I finally accomplished the most important and meaningful change in my life.

Finally, the deepest thanks go to my family, my parents, my mentor, and her.

CHAPTER 1

INTRODUCTION

1.1 Background and Objective

The growing need for high performance and wide bandwidth handheld mobile devices capable of operating at various communication bands necessitates use of microelectromechanical system (MEMS) resonators having simultaneous high resonance frequency (f_o), high quality factor (Q) and high electromechanical coupling as building blocks. These well-known but mostly competing requirements have driven research efforts on different transduction mechanisms. Among these, piezoelectric and film bulk acoustic resonators (FBAR) have achieved electromechanical coupling coefficients larger than 6%, but their Qs are smaller than desired [1].

Higher Q would provide lower insertion loss. There is no doubt that MEMS capacitive-gap transduced resonators can achieve high on-chip quality factors from high frequency (HF, $3 - 30$ MHz) to very high frequency (VHF, $30 - 300$ MHz) and even to ultra-high frequency (UHF, 300 MHz $- 3$ GHz), with Q values reaching 98,000 at 73 MHz [2] and 40,000 at 2.97 GHz [3]. Lots of well-known applications with low insertion loss and low power consumption are based on this technology, for instance, a 0.09% bandwidth 223.4 MHz channel-select filters with only 2.7dB of in-band insertion loss and 50dB of out-of-channel interferer rejection [4], a 78 mW GSM phase noise-compliant pierce oscillator [5], a squegging micromechanical clock generator with only 0.8 nW of battery power [6].

However, there is a strong trade-off between frequency and electromechanical coupling gauged by the motional-to-static capacitive ratio (C_x/C_o) in capacitive-gap transduced resonators. This ratio represents the efficiency of energy transfer between the electrical and mechanical domains [7]. It determines the percent bandwidth of a micromechanical filter [8] and the tuning range of the resonance frequency [9]. At HF, the coupling is strong enough, with C_x/C_o reaching 30% [8]. While in VHF and UHF devices mentioned above, C_x/C_o are much lower. Resonators with capacitive-gap transduced mechanism still struggle to achieve both high frequency and high C_x/C_o. A primary industrial requirement is $C_x/C_o \geq 6\%$ at $f_o \geq 700$ MHz. With proper design, the strong electromechanical coupling should be achievable at UHF.

Pursuant to unleashing this potential, any decent approach should first determine the effect of various design and material parameters on electromechanical coupling. The motional-to-static capacitive ratio for a resonator with a fully surrounded electrode is given by

$$\frac{C_x}{C_o} = \frac{\varepsilon_o A_o V_P^2}{(2\pi f_{nom})^2 m_m d_o^3} \tag{1.1}$$

where C_x is the motional capacitance of the resonator, C_o is the static capacitance, ε_o is the vacuum permittivity, A_o is the overlap area between the electrode and the resonator, V_P is the DC bias voltage, f_{nom} is the nominal frequency, m_m is the dynamic mass, d_o is the electrode-to-resonator gap. From this expression, larger C_x/C_o requires large overlap area, large DC bias voltage and small gap spacing.

Many research efforts went into different ways to reduce the electrode-to-resonator gap. Post ALD partial refilled gap lowered the effective gap down to 37 nm and achieved C_x/C_o around 0.58% at 61 MHz [10]. Simply reducing the gap with a better etching recipe shrunk the gap as small as 13 nm and strengthened C_x/C_o up to 1.62% at 60 MHz [7]. Both works are astonishing, undoubtedly, but none of them approaches the industrial requirement and there is not enough room for shrinking the gap with today's fabrication capability even for integrated circuits [11]. In addition, there is a strong tradeoff between the gap spacing and the DC bias due to the pull-in issue. Besides, the yield will degrade when a very tiny gap exists on a wafer. In addition, surface micromachining limits the overlap area of a disk resonator, for instance, limited deposition thickness and limited etching selectivity. Thus, to explore more potentials from Equation (2.1) m_m is the only parameter waiting to be improved.

Hollowing out a disk resonator is an intuitive approach to reduce m_m at VHF and even UHF because of less dynamic mass. One decent property of a disk resonator is that the nominal frequency is only determined by the lateral dimension (i.e., the radius of the disk, R) instead of its vertical geometry (i.e., thickness, t) [9]. A hollow disk can boost its C_x/C_o, and its frequency will stay at the same level.

There are many ways to make a hollow disk, and this thesis introduces two types of hollow structures: asymmetric and symmetric. Figure 1.1 presents their cross-section views. It is easier to fabricate an asymmetric hollow disk, where a thin sidewall ring protrudes upward from the edges of an inner disk. The radial vibration of the sidewall enhances C_x/C_o boosting, but it has more nonidealities, including the transvers vibration of the inner disk. A symmetric hollow disk, in which the sidewall ring protrudes in both upwards and downwards directions, can eliminate vertical vibration nonidealities because it is more symmetric in the vertical direction. However, a step of timed etch is required in fabricating this disk.
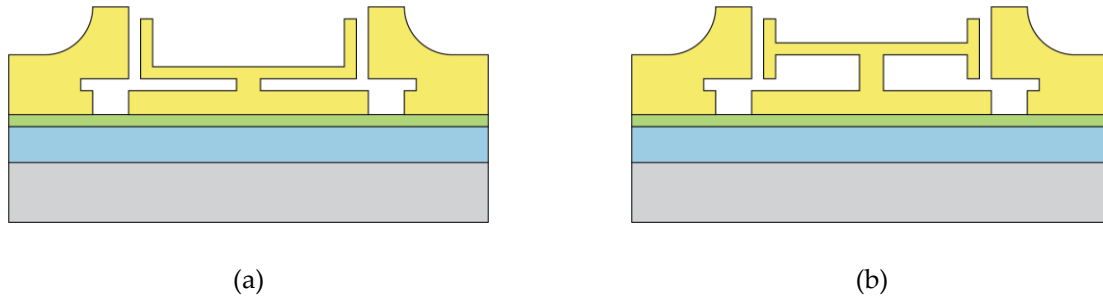
Figure 1.1: Schematic showing cross-section views of (a) an asymmetric hollow disk and (b) a symmetric hollow disk

1.2 Thesis Overview

This thesis explores a method that raises C_x/C_o by hollowing out a disk resonator structure. Chapters 2 and 3 introduce two types of hollow disk design: asymmetric and symmetric respectively.

In Chapter 2, Section 2.1 introduces an asymmetric hollow disk and its negative capacitance equivalent circuit. Section 2.2 analyzes the transverse vibration nonideality in the hollow disk by finite element analysis (FEA). Section 2.3 creates a new radial cantilever model for the sidewall ring. Section 2.4 shows a new fabrication process yielding this device. Finally, Section 2.5 proves the entire modeling and simulation in previous sections by device measurements.

In Chapter 3, Section 3.1 introduces a more symmetric hollow disk and its performance. Section 3.2 introduces a large-stemmed symmetric hollow disk, because this is the only testable one because of post-fabrication stress gradients. Section 3.3 shows a slightly different fabrication process yielding this device. Measurement results in Section 3.4 further confirm the entire modeling and simulation.

Chapter 4 concludes the above research and provides a view on the future research.

CHAPTER 2

ASYMMETRIC HOLLOW DISK

2.1 Asymmetric Hollow Disk Design and Equivalent Circuit

To prove the new method of hollow disk electromechanical coupling C_x/C_o boosting, Figure 2.1 schematically shows an 80 MHz asymmetric hollow radial contour disk with a fully surrounded electrode, in which a thin sidewall ring protrudes upward from the edges of an inner disk that itself anchors to the substrate via a center stem. A few nonidealities influence this asymmetric structure, for instance, transverse vibration of the inner disk and reduction of the nominal frequency.
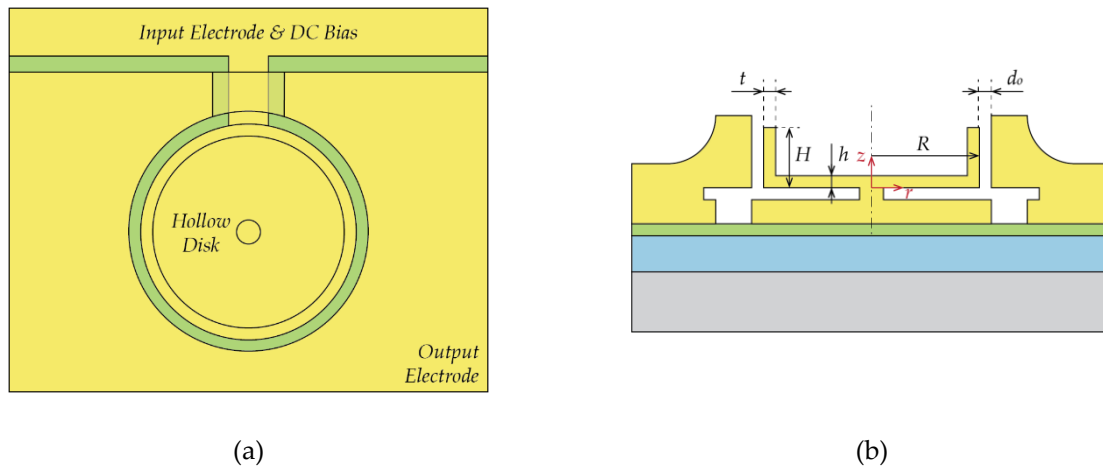

| (a) | (b) |

Figure 2.1: Schematic showing an asymmetric hollow disk with a fully surrounded electrode and variables used in derivation: (a) top view and (b) cross-section view

Negative capacitance equivalent circuits in [9] can correctly model capacitive-gap transduced resonators, including hollow disks. Figure 2.2 presents two equivalent circuits of the device in Figure 2.1. In Figure 2.2 (a), the LCR circuit (i.e., l_x, c_x and r_x) represents the resonator in the mechanical domain, and a static capacitor (C_o) is in parallel with it in the electrical domain. In Figure 2.2 (b), the electromechanical coupling ratio (η_e) converts all mechanical variables to the

electrical domain, where a negative capacitor $(-C_e)$ is equivalent to the negative electrical stiffness (k_e).
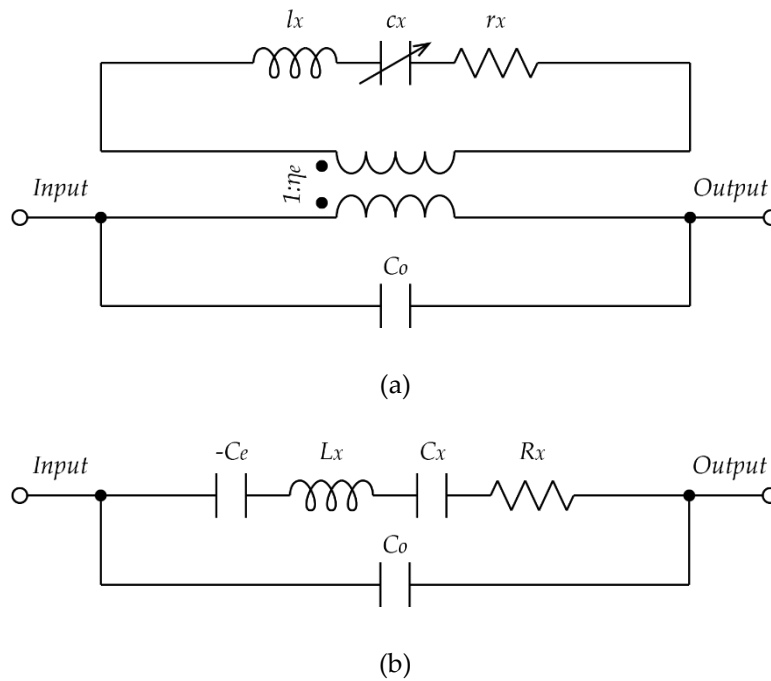

(a)

(b)

Figure 2.2: Equivalent circuits of a hollow disk with a fully surrounded electrode: (a) in the mechanical and electrical domains; (b) in the electrical domain

Table 2.1 summarizes detailed design and equivalent circuit variables of the 80 MHz asymmetric hollow disk. All geometric dimensions of the structure (i.e., R, H, h, t, and d_o) are from measurements in Section 2.4, including material thickness and profile measurements. Results from device measurement in Section 2.5 yield the rest design variables (i.e., V_P, Q, f_{nom}, and f_o). Finite element analysis (FEA) can extract all equivalent circuit variables directly. The mechanical inductance (l_x) of the hollow disk is only 38% of the solid disk. The electromechanical coupling ratio (η_e) of the hollow disk is 66% higher than the solid one. As a result, the motional-to-static capacitive ratio (C_x/C_o) can be boosted by approximately ten times and the motional resistance (R_x) is 87% lower.

Figure 2.3 presents simulated mode shapes of the asymmetric hollow disk and a similar frequency solid disk in Table 2.1. According to Figure 2.3 (a), the inner disk vibrates not only radially but also transversely. Additionally, the thin sidewall tends to vibrate radially in evidence. This type of vibration is similar to a cantilever, which is the so-called radial cantilever mode in Section 2.4.

Table 2.1: Summary of detail design and equivalent circuit variables of the 80 MHz asymmetric hollow disk and a 80 MHz solid disk

	Parameters	Solid Disk	Hollow Disk	Units
Design Variables	Disk Radius (outer), R	32.35	32.35	μm
	Total Height, H	2.4	2.4	μm
	Inner Disk Thickness, h	--	600	nm
	Sidewall Thickness, t	--	350	nm
	Electrode-to-Resonator Gap, d_o	148	148	nm
	DC Bias Voltage, V_P	20	20	V
	Quality Factor, Q	5000	5000	--
	Nominal Frequency, f_{nom}	81.637	79.601	MHz
	Resonance Frequency, f_o	81.631	79.450	MHz
Equivalent Circuit Variables	Mech. Inductance (mass), l_x	13.850	5.288	pH
	Mech. Capacitance (1/stiffness), c_x	0.274	0.756	μF
	Mech. Resistance (damping), r_x	1.421	0.529	μΩ
	Static Overlap Capacitance, C_o	29.185	29.185	fF
	Electromechanical Coupling Ratio, η_e	3.944	6.582	μC/m
	Motional Inductance, L_x	0.890	0.122	H
	Motional Capacitance, C_x	0.004	0.033	fF
	Motional Resistance, R_x	91.348	12.210	kΩ
	Electrical Stiffness Equiv. Cap., $-C_e$	-29.185	-9.412	fF
	C_x-to-C_e Capacitive Ratio, C_x/C_e	0.015	0.384	%
	C_x-to-C_o Capacitive Ratio, C_x/C_o	0.015	0.142	%

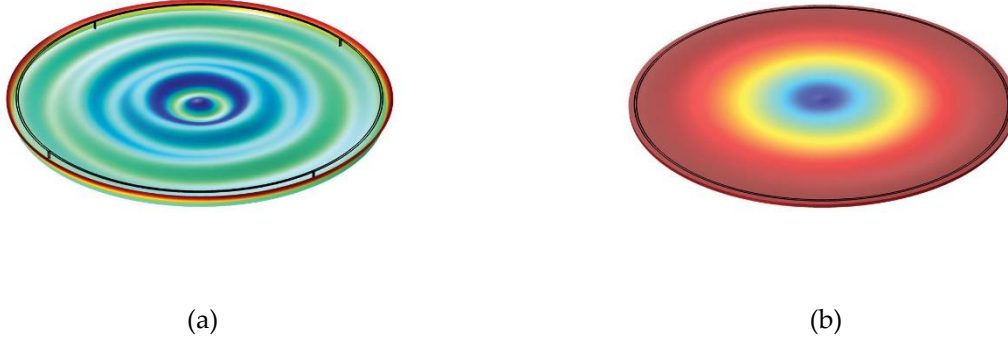<p style="text-align:center">(a)   (b)</p>

Figure 2.3: Simulated mode shapes of (a) the 80 MHz asymmetric hollow disk and (b) the solid disk in Table 2.1

FEA can generate surface and volume integrations directly from a simulated mode shape. Subsequently, these integrations can yield all equivalent circuit variables in Figure 2.2 (a).

A volume integration can yield the total dynamic mass (m_m) or mechanical inductance (l_x) by

$$l_x = m_m = \frac{\iiint ([R_{mode}(r,\theta,z)]^2 + [Z_{mode}(r,\theta,z)]^2)dm}{[R_{mode}(r_{ref},\theta_{ref},z_{ref})]^2}$$
$$= \frac{\rho \iiint ([R_{mode}(r,\theta,z)]^2 + [Z_{mode}(r,\theta,z)]^2)dV}{[R_{mode}(R,0,0)]^2} \quad (2.1)$$

where $R_{mode}(r,\theta,z)$ and $Z_{mode}(r,\theta,z)$ are the simulated radial and vertical mode shape functions of the entire structure respectively, $\iiint ([R_{mode}(r,\theta,z)]^2 + [Z_{mode}(r,\theta,z)]^2)dV$ is the volume integration based on these two functions, $R_{mode}(r_{ref},\theta_{ref},z_{ref})$ is the radial displacement at the chosen reference point (i.e., $r_{ref} = R, \theta_{ref} = 0, z_{ref} = 0$), and R is the outer radius of the hollow disk. The dynamic stiffness (k_m) and damping (b_m) yield the mechanical capacitance (c_x) and resistance (r_x),

$$c_x = \frac{1}{k_m} = \frac{1}{(2\pi f_{nom})^2 m_m} \quad (2.2)$$

$$r_x = b_m = \frac{\sqrt{k_m m_m}}{Q} \quad (2.3)$$

where f_{nom} is the nominal frequency, and Q is the quality factor. The static capacitance across the electrode-to-resonator gap (d_o) is

$$C_o = \frac{2\pi\varepsilon_o RH}{d_o} \tag{2.4}$$

where ε_o is the vacuum permittivity, and H is the total height of the hollow disk. The electromechanical coupling ratio is given by

$$\eta_e = \frac{V_P \lambda C_o}{d_o} \tag{2.5}$$

where λ is the nonlinear coefficient which can be extracted from a surface integration of the simulated radial mode shape function of the sidewall ($R_{mode}(R, \theta, z)$),

$$\lambda = \frac{1}{2\pi RH} \frac{\iint R_{mode}(R, \theta, z)dS}{R_{mode}(R, 0, 0)} \tag{2.6}$$

and where $R_{mode}(R, 0, 0)$ is from the same reference point. Convert mechanical variables to the electrical domain by η_e,

$$L_x = \frac{l_x}{\eta_e^2}, \quad C_x = c_x \eta_e^2, \quad R_x = \frac{r_x}{\eta_e^2} \tag{2.7}$$

Mechanically, the DC bias introduces a negative electrical stiffness ($-k_e$), which shifts the resonance frequency (f_o) from the nominal frequency (f_{nom}),

$$f_o = f_{nom}\sqrt{\frac{k_m - k_e}{k_m}} \tag{2.8}$$

$-1/k_e$ is equivalent to a negative capacitor ($-C_e$) in the electrical domain as shown in Figure 2.2 (b) by

$$k_e = \frac{\eta_e^2}{C_e} = k_m \frac{C_x}{C_e} \tag{2.9}$$

Substitute Equation (2.9) in (2.8),

$$f_o = f_{nom}\sqrt{\frac{k_m - k_e}{k_m}} = f_{nom}\sqrt{\frac{1/C_x - 1/C_e}{1/C_x}} = f_{nom}\sqrt{1 - \frac{C_x}{C_e}} \tag{2.10}$$

Rearrangement yields the expression for C_x/C_e,

$$\frac{C_x}{C_e} = \frac{f_{nom}^2 - f_o^2}{f_{nom}^2} \tag{2.11}$$

8

On the other hand, Figure 2.2 (b) presents another equivalent circuit in the electrical domain. For simplicity, combine C_x and $-C_e$ as C_x',

$$C_x' = C_x \parallel (-C_e) = \frac{C_x C_e}{C_e - C_x} \tag{2.12}$$

The total impedance is the LCR and C_o in parallel, which is also the transfer function of the circuit,

$$Z = \left(sL_x + \frac{1}{sC_x'} + R_x\right) \parallel \left(\frac{1}{sC_o}\right) = \frac{1}{sC_o} \frac{s^2 L_x C_x' + sR_x C_x' + 1}{s^2 L_x C_x' + sR_x C_x' + 1 + \frac{C_x'}{C_o}} \tag{2.13}$$

Extract the numerator (N) and denominator (D) for frequency analysis,

$$N = s^2 L_x C_x' + sR_x C_x' + 1 = (1 - \omega^2 L_x C_x') + j\omega R_x C_x' \cong 1 - \omega^2 L_x C_x' \tag{2.14}$$

$$D = s^2 L_x C_x' + sR_x C_x' + 1 + \frac{C_x'}{C_o} = \left(1 + \frac{C_x'}{C_o} - \omega^2 L_x C_x'\right) + j\omega R_x C_x' \tag{2.15}$$

$$\cong 1 + \frac{C_x'}{C_o} - \omega^2 L_x C_x'$$

where the imaginal term is negligible if $Q > 10$. Minimizing N and D yields the series (or resonance, ω_o) and parallel (ω_p) frequencies respectively,

$$\omega_o = \sqrt{\frac{1}{L_x C_x'}} \tag{2.16}$$

$$\omega_p = \sqrt{\frac{1 + \frac{C_x'}{C_o}}{L_x C_x'}} \tag{2.17}$$

Substituting Equation (2.12) in (2.16) and (2.17) yields

$$\omega_o = \sqrt{\frac{1}{L_x C_x'}} = \sqrt{\frac{1}{L_x \frac{C_x C_e}{C_e - C_x}}} = \sqrt{\frac{1}{L_x C_x}} \sqrt{1 - \frac{C_x}{C_e}} = \omega_{nom} \sqrt{1 - \frac{C_x}{C_e}} \tag{2.18}$$

$$\omega_p = \sqrt{\frac{1 + \frac{C_x'}{C_o}}{L_x C_x'}} = \sqrt{\frac{1 + \frac{1}{C_o} \frac{C_x C_e}{C_e - C_x}}{L_x \frac{C_x C_e}{C_e - C_x}}} = \sqrt{\frac{1}{L_x C_x}} \sqrt{1 - \frac{C_x}{C_e} + \frac{C_x}{C_o}} = \omega_{nom} \sqrt{1 - \frac{C_x}{C_e} + \frac{C_x}{C_o}} \tag{2.19}$$

where the nominal frequency is,

$$\omega_{nom} = \sqrt{\frac{1}{L_x C_x}} \tag{2.20}$$

Thus, rearrangement and simplification of Equations (2.18) and (2.19) yields the expression for C_x/C_o,

$$\frac{C_x}{C_o} = \frac{\omega_p^2 - \omega_o^2}{\omega_p^2} = \frac{f_p^2 - f_o^2}{f_p^2} \tag{2.21}$$

According to Equation (2.19), the parallel frequency (f_p) will equal the nominal frequency (f_{nom}) only if $C_e = C_o$. Compare Equations (2.11) and (2.21), and these two capacitive ratios will be the same only if $C_e = C_o$. However, C_e does not equal C_o as [9] in this hollow disk. Section 2.5 will discuss this phenomenon in depth.

The hollow disk should vibrate in the radial contour mode. According to Figure 2.3 (a), however, it is the most critical nonideality that the inner disk vibrates not only in the desired radial direction but also in the undesired vertical direction, especially near the stem. With such disturbing transverse vibration, it is hard to determine whether the hollow disk vibrates in the radial contour mode. Based on the simulated mode shape in Figure 2.3 (a), solid lines in Figure 2.4 present the separated mode shape functions in the radial and vertical directions (i.e., R_{mode} and Z_{mode}). For purposes of comparison, dashed lines show the mode shape functions of an ideal solid disk. Now, it becomes much easier to confirm that the inner disk still vibrates in the radial contour mode in the radial direction because the solid blue line follows the dashed blue line although there is a small ripple. However, the transverse vibration of the inner disk is severe (i.e., solid orange line) compared to the solid disk (i.e., dashed orange line). Section 2.2 will analyze this nonideality in detail.

In Figure 2.3 (a), the sidewall also vibrates in the radial direction. Figure 2.5 presents this phenomenon more clearly. The blue line is the simulated radial mode shape function of the sidewall. For comparison, the displacement along the sidewall of the solid disk is uniform according to the orange line. Section 2.3 will have a more detailed analysis of this phenomenon.

To quantify the abovementioned effects, including the transverse vibration of the inner disk and the radial vibration of the sidewall, kinetic energies in the radial and vertical directions (i.e., RKE_i and VKE_i) of each part (i.e., $i = disk, sidewall, total$) can be derived from volume integrations based on the simulated mode shape functions,

$$RKE_i = \frac{1}{2}\rho \iiint_i [R_{mode}(r,\theta,z)]^2 dV \tag{2.22}$$

$$VKE_i = \frac{1}{2}\rho \iiint_i [Z_{mode}(r,\theta,z)]^2 dV \tag{2.23}$$

The total energy of each part is the sum of RKE_i and VKE_i,

$$TKE_i = RKE_i + VKE_i \tag{2.24}$$

Table 2.2 presents the kinetic energy distribution of each part during vibration. Thus, according to the result, the radial contour mode of the inner disk accounts for 71.70% in total energy. One nonideality, the transverse vibration of the inner disk, comprises 16.08%. Another phenomenon, the radial vibration of the sidewall, makes up 12.16%. The vertical vibration of the sidewall is negligible since it is only 0.06%.
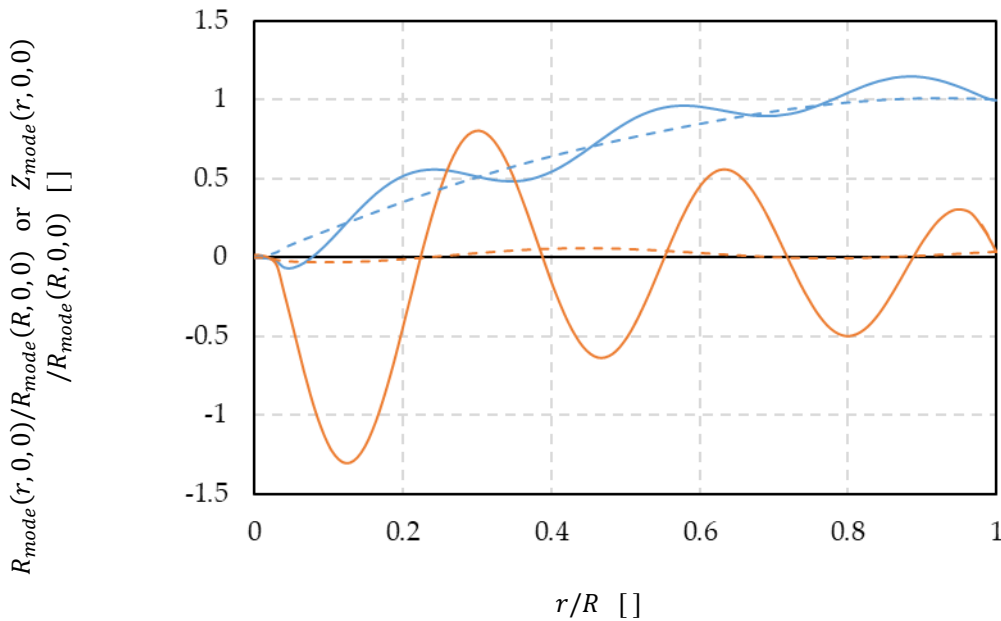
Solid blue/orange line: radial/vertical mode shape function of the inner disk of the hollow disk

Dashed blue/orange line: radial/vertical mode shape function of the solid disk

Figure 2.4: Simulated normalized radial and vertical mode shape functions of the inner disk of the hollow disk and the solid disk
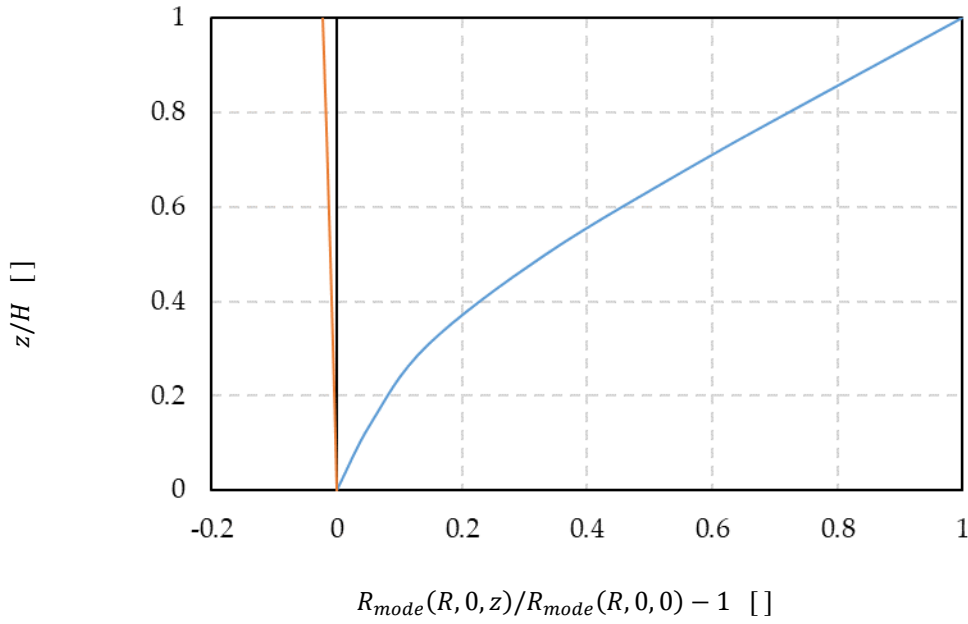
Blue: the sidewall of the hollow disk; Orange: the sidewall of the solid disk

Figure 2.5: Simulated normalized radial mode shape functions of sidewalls of the hollow disk and the solid disk

Table 2.2: Kinetic energy distribution of each part during vibration

Parts	Radial K.E. (i.e. RKE_i)	Vertical K.E. (i.e. VKE_i)	Total K.E. (i.e. TKE_i)
$i = disk$	71.70%	16.08%	87.78%
$i = sidewall$	12.16%	0.06%	12.22%
$i = total$	83.86%	16.14%	100%

Section 2.2 and 2.3 will investigate these phenomena in detail.

2.2 Finite Element Analysis of the Transverse Vibration

In Table 2.1, the inner disk thickness (h) and total height (H) of the designed 80 MHz asymmetric hollow disk are 0.6 μm and 2.4 μm respectively. A new parameter h/H defines the

12

hollowness of a hollow disk, so the hollowness of the 80 MHz hollow disk is $h/H = 0.25$. The smaller the value of h/H is, the hollower the disk is. As h/H reaches to one, the hollow disk becomes a solid one.

Two critical phenomena exist in an asymmetric hollow disk, the transverse vibration of the inner disk and the radial vibration of the sidewall, by analyzing mode shape functions and quantifying by kinetic energy distribution. Now, we are focusing on the effect of h/H on the transverse vibration.
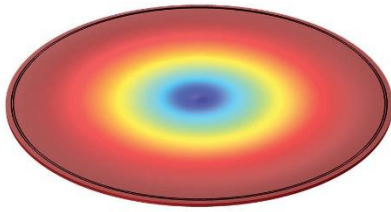
Figure 2.6 presents mode shapes of hollow disks with various h/Hs, where h is 0.6 μm, and H varies from 0.6 μm to 3 μm. As h/H reaches to one, the hollow disk, which becomes a solid disk, vibrates in the ideal radial contour mode. The transverse vibration nonideality becomes very severe while h/H is only 0.2. It is hard to determine whether the inner disk still vibrates in the radial contour mode in the radial direction.

Figure 2.7 and 2.8 present simulated radial and vertical mode shape functions of inner disks in hollow disks with various h/Hs respectively. In Figure 2.7, even when h/H is approaching 0.2, the radial mode shape function of the inner disk still follows the ideal radial contour mode shape function, although there is nonideal undulation. However, the nonideal transverse vibration becomes more obvious in Figure 2.8.

To quantify this nonideality, Figure 2.9 presents the effect of h/H on the vertical kinetic energy of the inner disk. The severity of the transverse vibration goes above 12% when $h/H <$ 0.25 and reaches 45% when $h/H = 0.2$. It becomes very sensitive to h/H when h/H is small.

As shown in Figure 2.6, the nominal frequency decreases with decreasing h/H. To visualize this effect, Figure 2.12 presents the frequency degradation from the simulation. The hollow shape lowers the nominal frequency by more than 4.7% when $h/H < 0.25$ and up to 10% when $h/H = 0.2$.

Overall, the transverse vibration nonideality of the inner disk, exists in asymmetric hollow disks and is not negligible. The hollower the disk is, the more severe and sensitive the nonideality is. The hollow shape also reduces the nominal frequency. For the hollow disk design with $h/H = 0.25$ in Table 2.1, the transverse vibration of the entire structure comprises 12%, its nominal frequency is lowered by 4.7%. If the disk is hollower with $h/H = 0.2$, the transverse vibration can make up 45% in total, and its frequency is only 90% of the original.
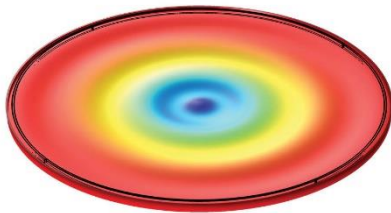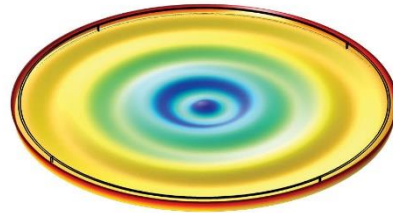
$f_{nom} = 81.657$ MHz

(a) $h/H = 1$
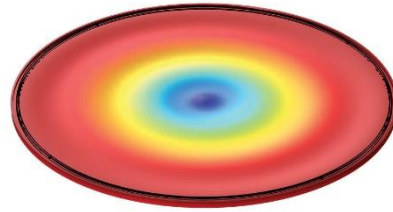
$f_{nom} = 80.761$ MHz

(b) $h/H = 0.5$

$f_{nom} = 80.273$ MHz
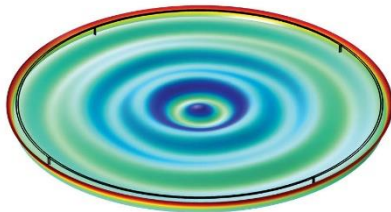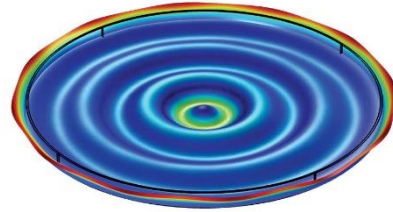
(c) $h/H = 0.4$

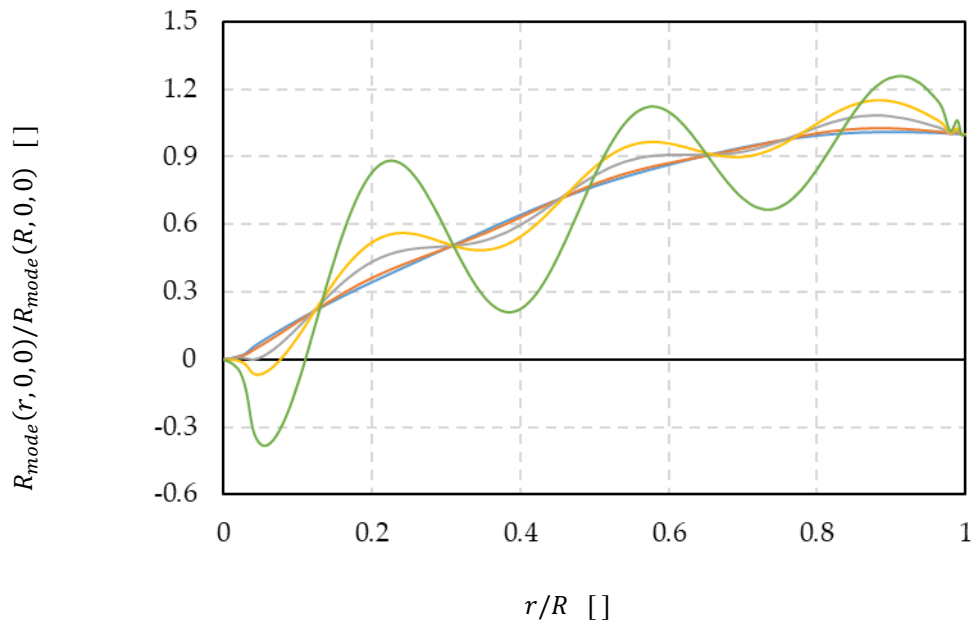$f_{nom} = 79.226$ MHz

(d) $h/H = 0.3$

$f_{nom} = 77.827$ MHz
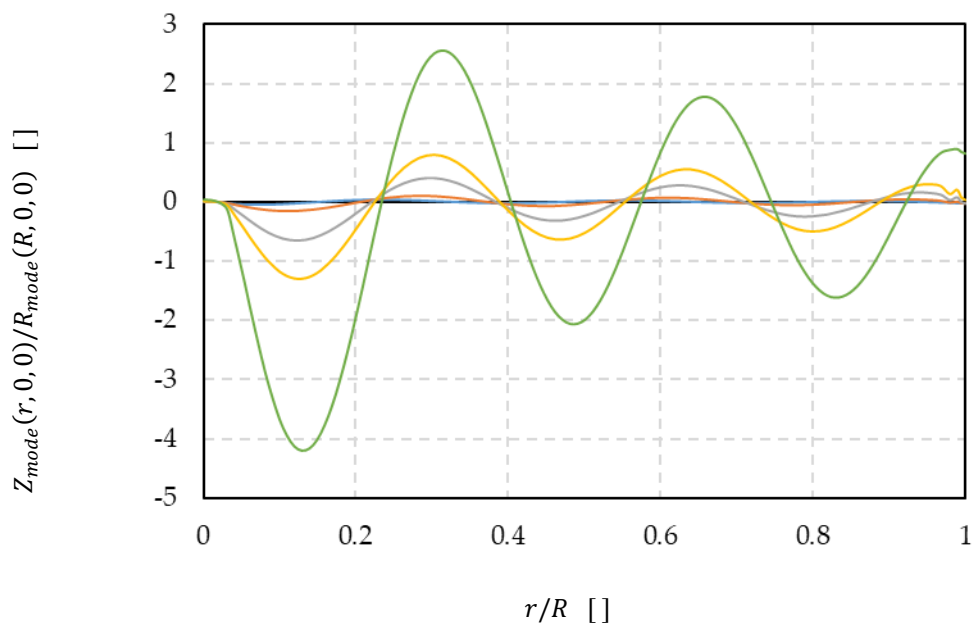
(e) $h/H = 0.25$

$f_{nom} = 73.167$ MHz

(f) $h/H = 0.2$

Figure 2.6: Mode shapes of hollow disks with various h/Hs

Blue: $h/H = 1$; Orange: $h/H = 0.5$; Gray: $h/H = 0.3$; Yellow: $h/H = 0.25$; Green: $h/H = 0.2$

Figure 2.7: Radial mode shape functions of inner disks with various h/Hs

Blue: $h/H = 1$; Orange: $h/H = 0.5$; Grey: $h/H = 0.3$; Yellow: $h/H = 0.25$; Green: $h/H = 0.2$

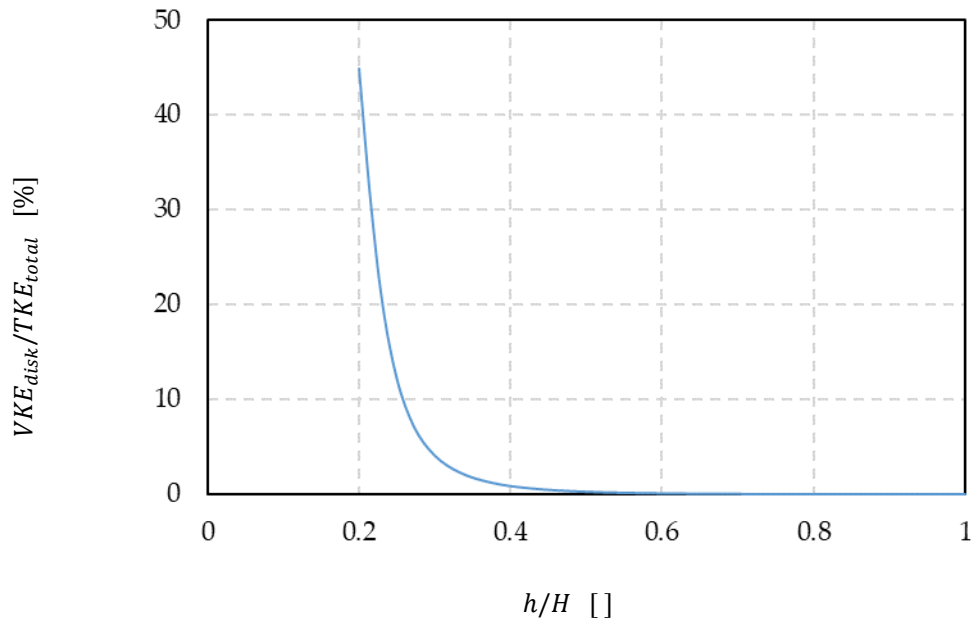Figure 2.8: Vertical mode shape functions of inner disks with various h/Hs

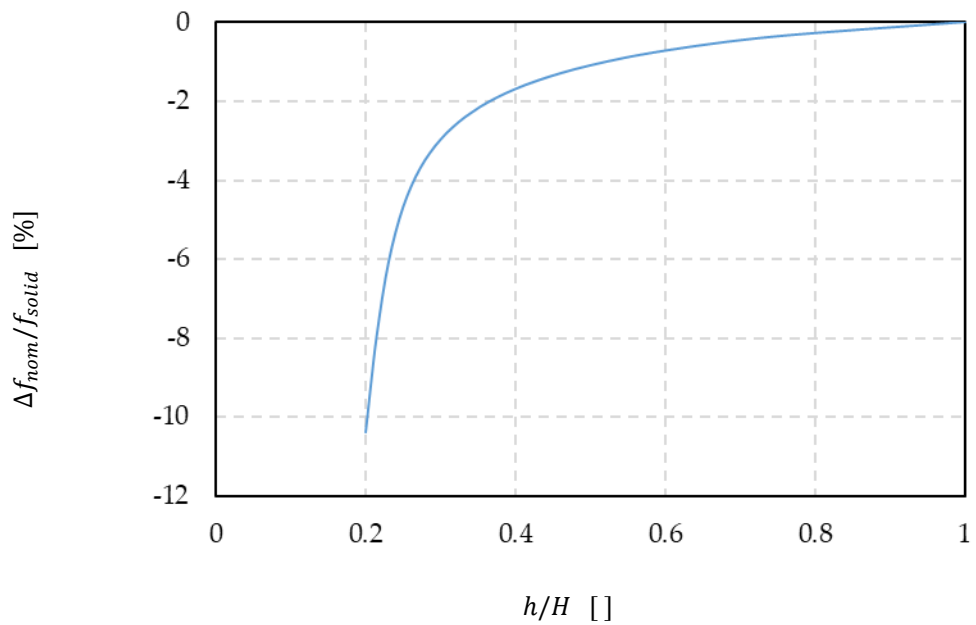Figure 2.9: Vertical kinetic energies of inner disks with various h/Hs

Figure 2.10: Simulated nominal frequency degradation with decreasing h/H

2.3 Radial Cantilever Model of the Sidewall Ring

Section 2.2 analyzed the effect of the asymmetric structure on the transverse vibration of the inner disk, and this section will analyze and model the radial vibration of the circular sidewall.

Figure 2.11 presents radial mode shape functions of sidewalls in hollow disks with various h/Hs. The radial vibration of the sidewall becomes more significant when the disk is hollower. This is a good property because it boosts C_x/C_o even higher.
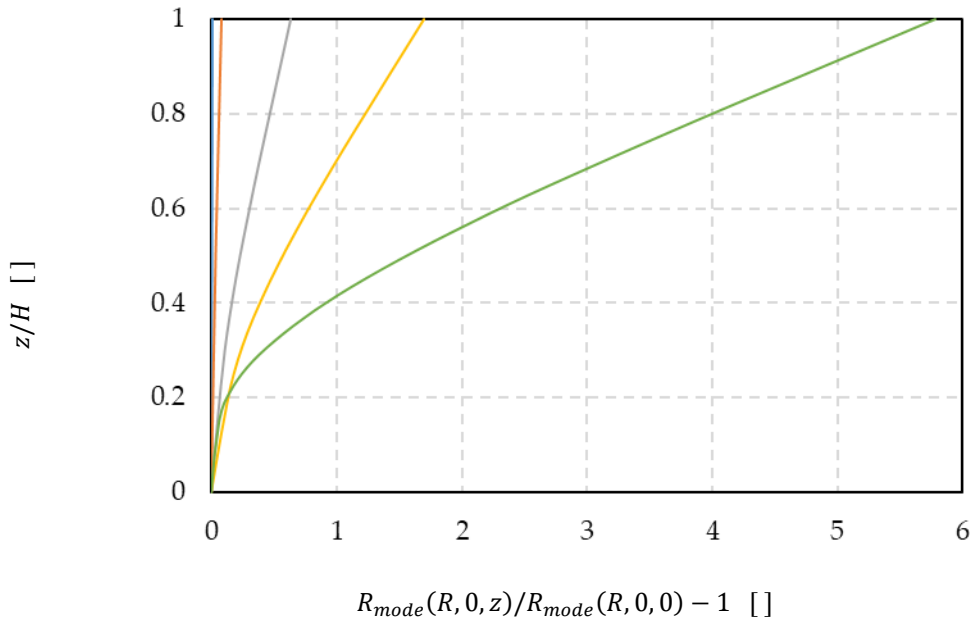
Blue: $h/H = 1$; Orange: $h/H = 0.5$; Grey: $h/H = 0.3$; Yellow: $h/H = 0.25$; Green: $h/H = 0.2$

Figure 2.11: Radial mode shape functions of sidewalls with various h/Hs

The radial vibration of the sidewall ring is similar to a radial cantilever, which is an infinite number of infinitely narrow cantilevers side by side in a circle, as shown in Figure 2.12. The main effect in the radial cantilever is the curvature effect that can boost the frequency from a simple cantilever but the mode shape stays the same.
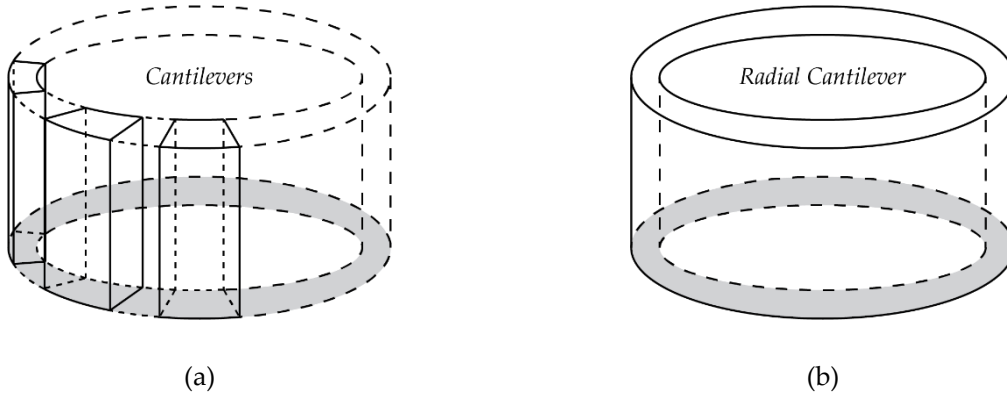
Figure 2.12: Schematic showing that connect (a) an infinite number of infinitely narrow cantilevers side by side in a circle to form (b) a radial cantilever

To derive the Euler Bernoulli beam equation for a radial cantilever, start from the equation of a simple cantilever,

$$EI\frac{\partial^4 r}{\partial z^4} = \rho S\omega^2 r \tag{2.25}$$

where r is the displacement function, ω is the resonance frequency, S is the cross-section area of the beam, and I is the moment of inertia. Figure 2.13 shows the directions of r-axis and z-axis.
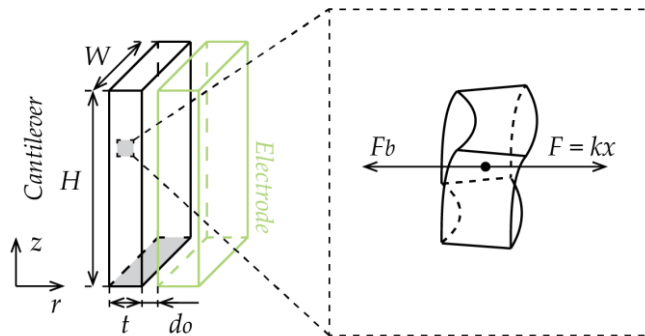

Figure 2.13: Schematic showing variables used in the Euler Bernoulli beam equation of a simple cantilever

The equation is just as simple as

$$F_b = F \tag{2.26}$$

where F_b is the force due to bending of each infinitely small segment, F is the inertia force,

$$F_b \propto EI\frac{\partial^4 r}{\partial z^4}, \quad F = k_c x \propto \rho S\omega^2 r, \tag{2.27}$$

and where k_c is the equivalent stiffness of each segment on the cantilever and x is the displacement function (i.e. $x = r$).

Given by boundary conditions of a cantilever,

$$
\begin{aligned}
r(z = 0) &= 0 \\
r'(z = 0) &= 0 \\
r''(z = H) &= 0 \\
r'''(z = H) &= 0
\end{aligned}
\tag{2.28}
$$

solving Equation (2.25) yields the resonance frequency and mode shape function of a simple cantilever,

$$f_{can} = 0.1615\sqrt{\frac{E}{\rho}\frac{t}{H^2}} \tag{2.29}$$

$$X_{mode}(z) = [\cos(\varphi z) - \cosh(\varphi z)] + \xi[\sin(\varphi z) - \sinh(\varphi z)] \tag{2.30}$$

where H is the length of the beam, t is the thickness, and constants ξ and φ are given by

$$\xi = -\frac{\cos(\varphi H) + \cosh(\varphi H)}{\sin(\varphi H) + \sinh(\varphi H)}, \quad \varphi H = 1.8751 \tag{2.31}$$

Figure 2.14 (a) shows the mode shape from simulation in 2D, and it matches Equation (2.31) perfectly.

Equivalently, a radial cantilever is an infinite number of infinitely narrow cantilevers connecting side by side in a circle, as shown in Figure 2.12. Figure 2.17 (b) presents its mode shape from FEA.

The Euler Bernoulli beam equation of a radial cantilever becomes,

$$EI\frac{\partial^4 r}{\partial z^4} + F_c' = \rho S\omega^2 r \tag{2.32}$$

where

19

$$I = \frac{Rd\theta t^3}{12}, \quad S = Rd\theta t \tag{2.33}$$

and where R is the outer radius of the radial cantilever, t is the thickness of the cantilever or sidewall, and F_C' is the curvature force per unit length in r direction due to the curvature effect, whose direction is opposite to the inertia force, as shown in Figure 2.15,

$$F_c' = \sigma_\theta t d\theta \tag{2.34}$$

where σ_θ is the stress in tangential direction or θ-direction generated by the curvature effect,

$$\sigma_\theta = E\epsilon_\theta \tag{2.35}$$

and where ϵ_θ is the strain in θ-direction given by

$$\epsilon_\theta = \frac{2\pi(R+r) - 2\pi R}{2\pi R} = \frac{r}{R} \tag{2.36}$$

and where r is the radial displacement function.

(a)   (b)
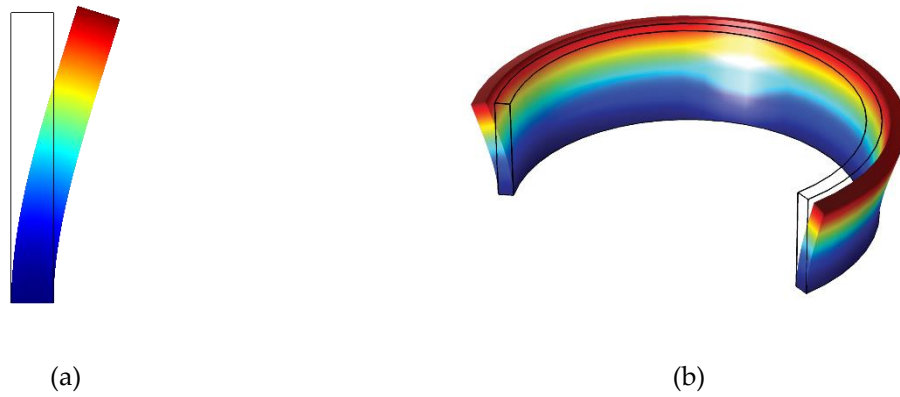
Figure 2.14: Simulated mode shapes of (a) a simple cantilever and (b) a radial cantilever

Compare Equation (2.32) with Equation (2.25). The curvature effect introduces a new force F_c, which is in the same direction as the bending force, so the equation is just as simple as

$$F_b + F_c = F = k_{rc}x \tag{2.37}$$

where k_{rc} is the equivalent stiffness of each segment on the radial cantilever, which must be larger than k_c due to the extra force F_c.
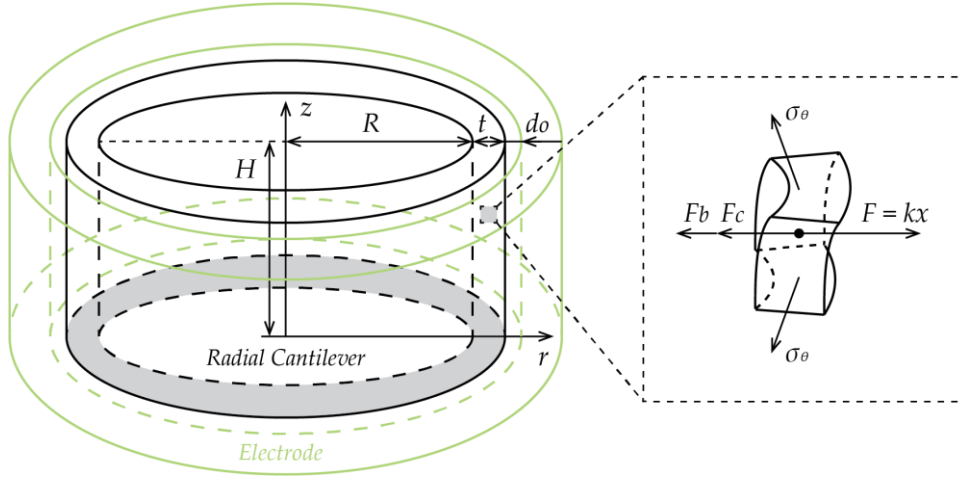
Figure 2.15: Schematic showing variables used in the Euler Bernoulli equation of a radial cantilever

Finally, Equation (2.32) becomes

$$E\frac{Rd\theta t^3}{12}\frac{\partial^4 r}{\partial z^4} + E\frac{r}{R}td\theta = \rho Rd\theta t\omega^2 r \tag{2.38}$$

To simplify the equation, rearrangement yields

$$\frac{\partial^4 r}{\partial z^4} = \left[\frac{12\rho\omega^2}{Et^2} - \frac{12}{R^2 t^2}\right]r \tag{2.39}$$

Solve the differential equations based on the same boundary conditions as Equations (2.28),

$$f_{rc} = \frac{1}{2\pi}\sqrt{\frac{E}{\rho}}\sqrt{1.0302\frac{t^2}{H^4} + \frac{1}{R^2}} \tag{2.40}$$

To provide better insight to variable dependencies, rearrangement and simplification yields the closed form

$$f_{rc} = 0.1615\sqrt{\frac{E}{\rho}}\frac{t}{H^2}\sqrt{1 + 0.9707\frac{H^4}{t^2 R^2}} = f_{can}\beta_c \tag{2.41}$$

21

where f_{can} is the frequency of a simple cantilever given by Equation (2.29) and β_c is the curvature coefficient given by

$$\beta_c = \sqrt{1 + 0.9707\frac{H^4}{t^2R^2}} \qquad (2.42)$$

Thus, with the same f_{can} (i.e. the ratio of t/H^2 is fixed), only the curvature radius (R) can boost f_{rc}. To visualize this effect, Figure 2.16 presents the effect of the curvature radius on the curvature coefficient from both Equation (2.42) and simulation, and they match each other perfectly. As the radius decreases, the frequency increases quadratically. As the radius goes to infinity, the frequency converges to the frequency of the simple cantilever where $\beta_c = 1$.
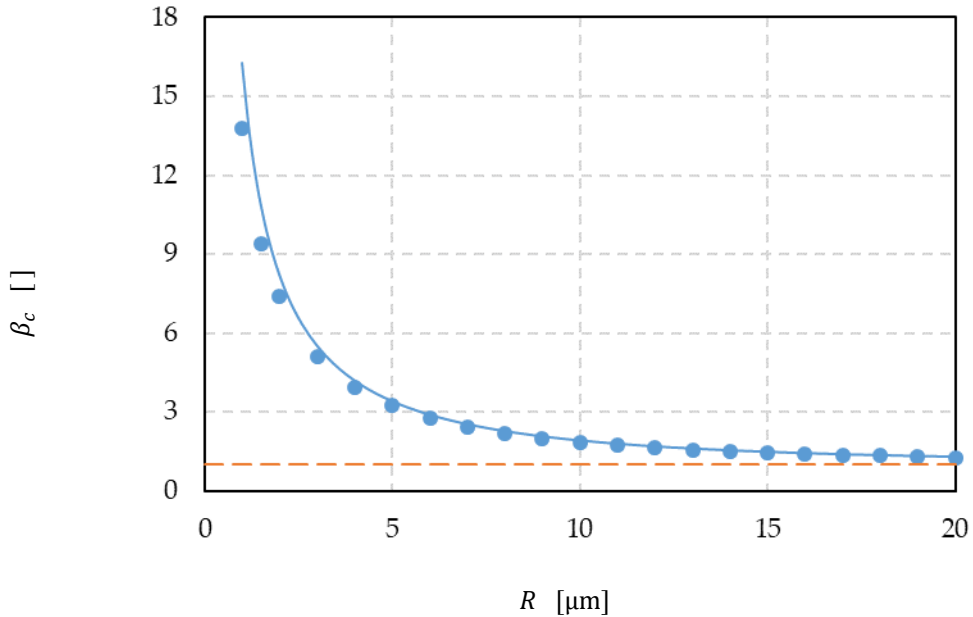
Blue line: model; Orange dots: simulation; Orange dashed line: $\beta_c = 1$

Figure 2.16: Curvature coefficient versus curvature radius

In addition, by solving Equation (2.38), the curvature effect does not affect the mode shape function. It is the same as Equation (2.30), which is the orange line in Figure 2.17. The blue line replots the simulated radial mode shape function of the circular sidewall in the 80 MHz asymmetric hollow disk for comparison. They match each other perfectly. Thus, the sidewall vibrates as a radial cantilever in the so-called radial cantilever mode.

Recall the nonlinear coefficient (λ) in Equation (2.5) calculating the electromechanical coupling ratio (η_e). It can be derived from not only the surface integration as Equation (2.16) but also the integration of the radial cantilever mode shape function (X_{mode}) in Equation (2.30). For a solid disk, since the sidewall vibrates uniformly, λ equals one. Due to the radial vibration of the circular sidewall, λ of the designed 80 MHz hollow disk becomes 1.669. As a result, in Table 2.1, η_e of the hollow disk is 6.582 μC/m, which is larger than 3.944 μC/m of the solid one. This is an advantage of hollow disks and one of the reasons they can boost C_x/C_o.

$R_{mode}(R, 0, z)/R_{mode}(R, 0, 0) - 1$ or $X_{mode}(z)/X_{mode}(H)$ [ ]
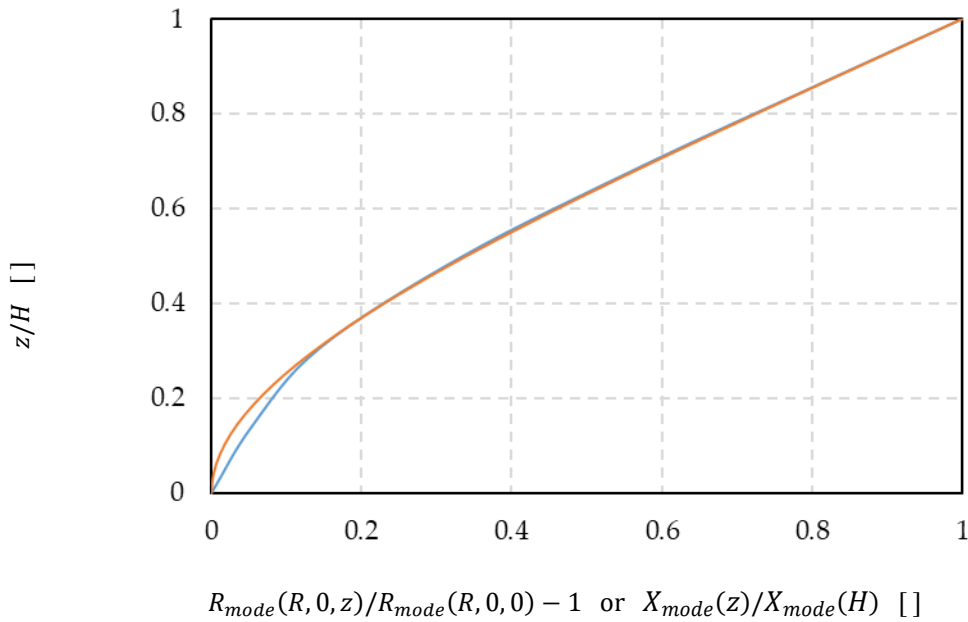
Blue: simulated radial mode shape function of the circular sidewall of the hollow disk;

Orange: modeled radial mode shape function of the radial cantilever

Figure 2.17: Normalized radial and vertical mode shape functions of a hollow disk and a solid disk from FEA

Furthermore, Table 2.3 presents the simulated nominal frequencies and mode shapes of the separated inner disk and sidewall in the designed 80 MHz hollow disk. The frequency of the inner disk is closer to the combined hollow disk, although the frequency of the sidewall is also not far away. The hollow disk combines two mode shapes, the radial contour and radial cantilever mode, with the nonideality of the transverse vibration.

Table 2.3: Comparison of the separated inner disk and sidewall with the combined hollow disk

	Isolated Inner Disk	Isolated Sidewall	Combined Hollow Disk
Nominal Frequency	81.637 MHz (from FEA)	91.548 MHz (from FEA)	79.601 MHz (from meas.) 77.829 MHz (from FEA)
Simulated Mode Shape	(radial contour)	(radial cantilever)	(combined)
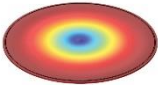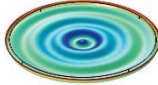
In conclusion, according to Section 2.2 and 2.3, the inner disk vibrates in the radial contour mode in the radial direction and the sidewall vibrates in the radial cantilever mode, while the inner disk also vibrates transversely, which is a critical nonideality lowering C_x/C_o. Hollow disk can boost C_x/C_o because of less dynamic mass and the radial vibration of the circular sidewall.

2.4 Fabrication Process

Figure 2.18 and Table 2.4 summarize the fabrication process yielding asymmetric hollow disks. This process flow follows the one yielding solid disk resonators in [9], but the most creative step is Step c-2, blank reactive ion etching (RIE) Si without a mask, where the anisotropic RIE leaves the sidewall.

Figure 2.19 (a) presents a scanning electron micrograph (SEM) of a fabricated asymmetric hollow disk with a fully surrounded electrode. Figure 2.21 (b) shows a tilted cross-section view of a dummy device after Step c-2, which shows the asymmetric hollow structure. The roughness of the sidewall after the blank etch is approximately 50 nm, which is larger than expected. It also limits the possibility of fabricating a very small gap in the subsequent Step d-1.

The process can make both the disk and the stem hollow as long as the stem is larger in Mask #2. As proved in [12], a higher quality factor is achievable in a disk resonator with a hollow stem. Figure 2.20 presents SEMs of a fabricated hollow disk with a hollow stem.

Figure 2.21 (a) presents a fabricated 148 nm gap spacing, while Figure 2.23 (b) shows the failure of the gap with a high DC bias voltage applied ($V_P > 20$ V) during measurement, in which the resonator and the electrode were shorted and the short current broke the hollow disk.

(a)

(b)

(c)

(d)

(e)

(f)

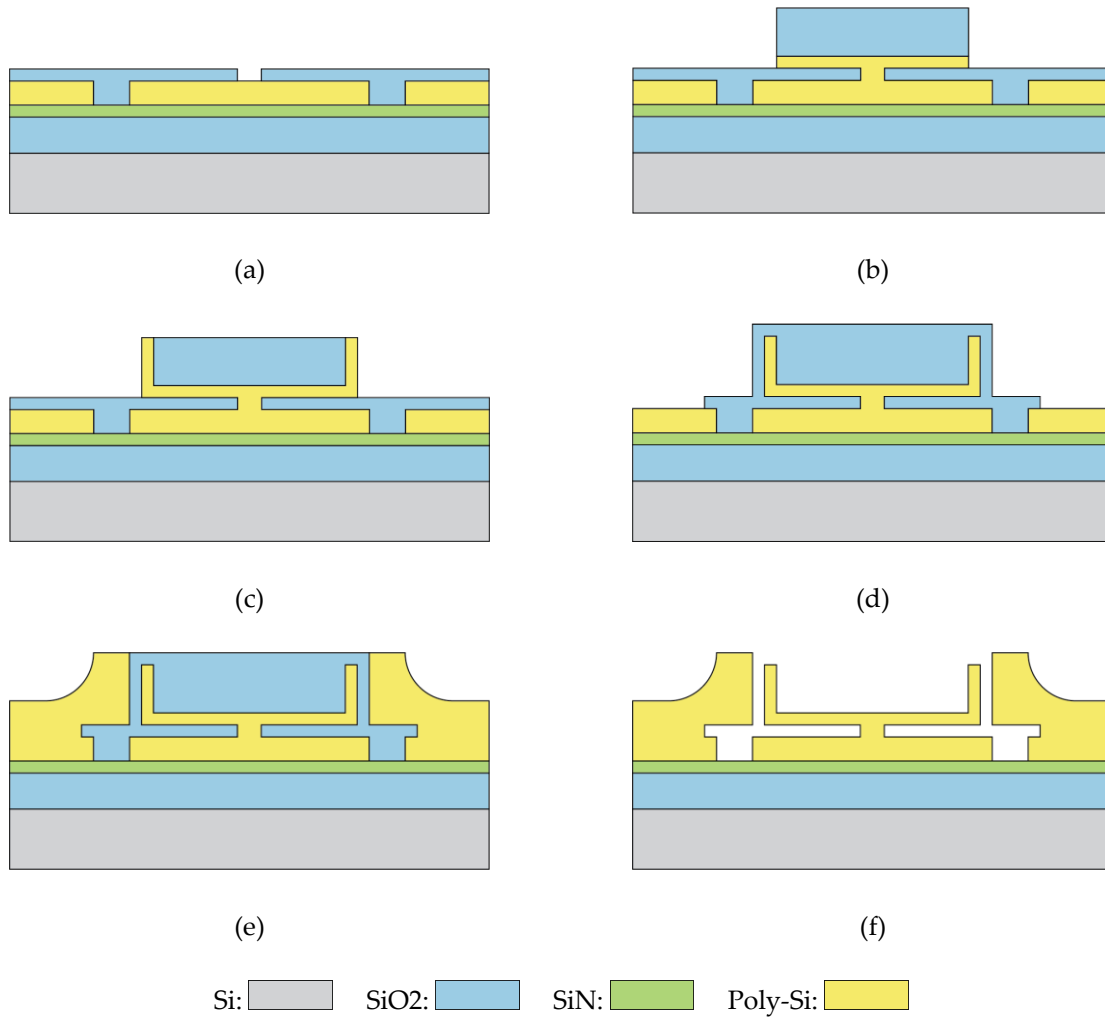Si: SiO2:   SiN: Poly-Si:

Figure 2.18: Fabrication process yielding asymmetric hollow disks with more detailed information shown in Table 2.5

Table 2.4: Detailed fabrication process yielding asymmetric hollow disks

Figure	Step	Fabrication	Details	Tools
(a)	a-1	Deposition	LPCVD 2 μm LTO	tyster 11 & 2
	a-2	Deposition	LPCVD 500 nm LSN	tyster 9
	a-3	Deposition	LPCVD 1 μm LTO	tyster 11 & 2
	a-4 (m1)	Patterning	RIE SiO$_2$ (by Mask #1, m1)	asml 300 & sts-oxide
	a-5	Deposition	LPCVD 1.5 μm Si (doped)	tyster 10 & 6
	a-6	CMP	CMP Si (stopped on SiO$_2$)	cmp
	a-7	Deposition	LPCVD 300 nm LTO	tyster 12 & 3
	a- 8 (m2)	Patterning	RIE SiO$_2$ (by Mask #2, m2)	asml 300 & sts-oxide
(b)	b-1	Deposition	LPCVD 600 nm Si (doped)	tyster 16 & 3
	b-2	Deposition	LPCVD 2 μm LTO	tyster 12 & 4
	b-3 (m3)	Patterning	RIE SiO$_2$ and Si (by Mask #3, m3)	asml 300 & sts-oxide & sts2
(c)	c-1	Deposition	LPCVD 350 nm Si (doped)	tyster 16 & 3
	c-2	Etching	Blank RIE Si (without a mask)	sts2
(d)	d-1	Deposition	LPCVD 148 nm HTO	tyster 17
	d-2 (m4)	Patterning	RIE SiO$_2$ (by Mask #4, m4)	asml 300 & sts-oxide
(e)	e-1	Deposition	LPCVD 3 μm Si (doped)	tyster 16 & 6
	e-2	CMP	CMP Si (stopped on SiO$_2$)	cmp
	e-3 (m5)	Patterning	RIE Si (by Mask #5, m5)	asml 300 & sts2
(f)	f-1	Release	HF Release	msink 18

Note: LPCVD: Low Pressure Chemical Vapor Deposition; RIE: Reactive Ion Etching; LTO: Low Temperature Oxide (SiO$_2$); LSN: Low Stress Nitride (Si$_x$N$_y$).
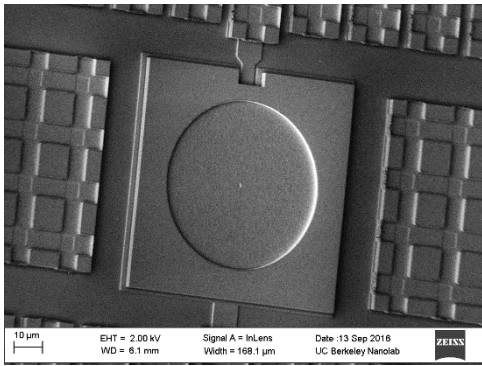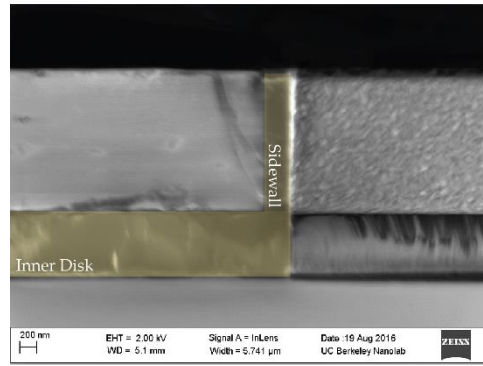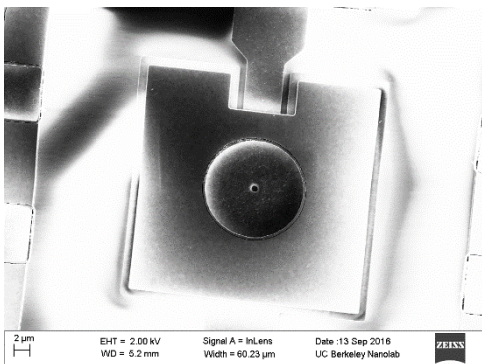
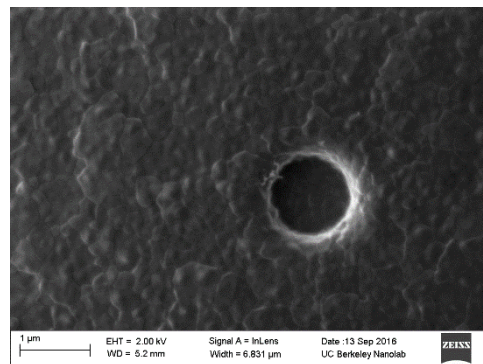(a)   (b)

Figure 2.19: SEMs of (a) a fabricated hollow disk with a fully surrounded electrode and (b) a tilted cross-section view of a dummy device after Step c-2
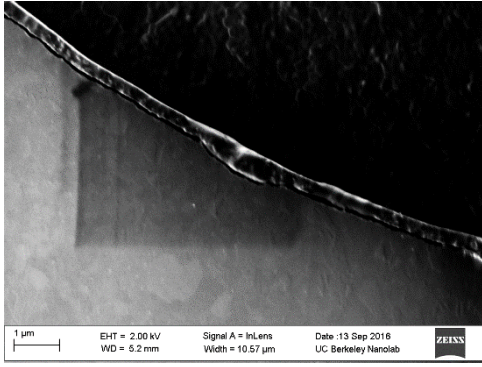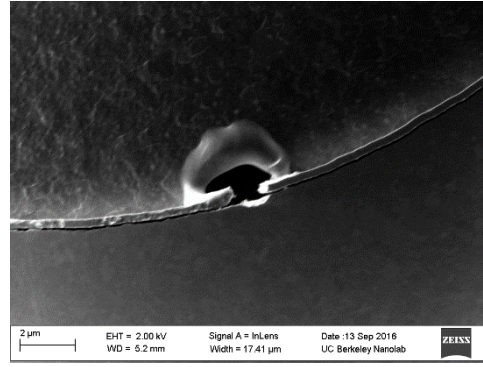

(a)   (b)

Figure 2.20: SEMs of (a) a fabricated hollow disk and (b) its hollow stem

Figure 2.21: SEMs of (a) the fabricated 80nm gap and (b) its failure with a high DC bias voltage applied

2.5 Measurement Results

This section will discuss measurement of the fabricated 80 MHz asymmetric hollow disk and characterization of the model in Section 2.1. Figure 2.22 presents the measured frequency responses with various DC bias voltages. They can directly yield the resonance (or series) and parallel frequencies (i.e., f_o and f_p) which are the frequencies of the maxima and minima respectively in the frequency response. The quality factor of this device is 5000.

Figure 2.23 presents measured resonance and parallel frequencies versus DC bias voltage (V_P). Both are dependent on V_P. To explain this phenomenon, recall Equation (2.18) and (2.19),

$$f_o = f_{nom}\sqrt{1 - \frac{C_x}{C_e}} \tag{2.43}$$

$$f_p = f_{nom}\sqrt{1 - \frac{C_x}{C_e} + \frac{C_x}{C_o}} \tag{2.44}$$

Because both capacitive ratios (i.e., C_x/C_e and C_x/C_o) are much smaller than 1, approximation yields

$$f_o = f_{nom}\sqrt{1 - \frac{C_x}{C_e}} \cong f_{nom}\left(1 - \frac{1}{2}\frac{C_x}{C_e}\right) \tag{2.45}$$

$$f_p = f_{nom} \sqrt{1 - \frac{C_x}{C_e} + \frac{C_x}{C_o}} \cong f_{nom} \left(1 - \frac{1}{2}\frac{C_x}{C_e} + \frac{1}{2}\frac{C_x}{C_o}\right) \qquad (2.46)$$

where C_o and C_e are voltage independent, but C_x is proportional to V_P^2. Linear regression of frequencies on V_P^2 yields

$$f_o = f_{nom} - \varphi_o V_P^2 = 79.603 \times 10^6 - 361.500 V_P^2 \qquad (2.47)$$

$$f_p = f_{nom} - \varphi_p V_P^2 = 79.609 \times 10^6 - 244.917 V_P^2 \qquad (2.48)$$

which are the blue and orange lines in Figure 2.23. Both lines yield approximately the same nominal frequency. Taking the ratio of two slopes yields

$$\kappa = \frac{\varphi_o}{\varphi_p} = 1.476 \qquad (2.49)$$

Taking the same ratio from Equation (2.45) and (2.46) yields

$$\kappa = \frac{\varphi_o}{\varphi_p} = \frac{\frac{1}{2}\frac{C_x}{C_e}}{\frac{1}{2}\frac{C_x}{C_e} - \frac{1}{2}\frac{C_x}{C_o}} = \frac{C_o}{C_o - C_e} \qquad (2.50)$$

Rearrangement yields

$$C_e = \frac{\kappa - 1}{\kappa} C_o = 0.322 C_o \qquad (2.51)$$

The negative capacitance equivalent circuit in [9] assumes $C_e = C_o$, but it is not accurate for this hollow disk. If it is true, f_p will equal f_{nom} and become voltage independent. C_e must not equal C_o, and Equation (2.51) can extract its value. For the asymmetric hollow disk in Table 2.1, C_e is 9.412 fF and C_o is 29.185 fF. As a result, C_x/C_e is 0.385% and C_x/C_o is 0.142% at $V_P = 20$ V. Both are much higher than $C_x/C_e = C_x/C_o = 0.015\%$ of the solid disk.

According to Equations (2.11) and (2.21), Figure 2.25 presents measured and modeled C_x/C_e and C_x/C_o. They match each other perfectly.
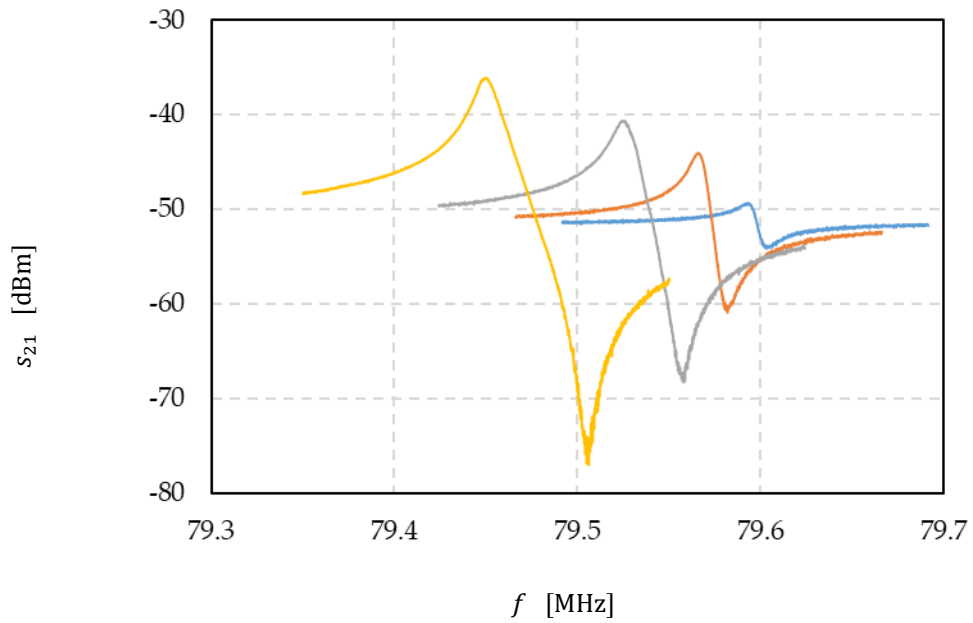
Yellow: $V_P = 20$ V; Gray: $V_P = 15$ V; Orange: $V_P = 10$ V; Blue: $V_P = 5$ V

Figure 2.22: Frequency responses of the 80 MHz hollow disk with various DC bias voltages
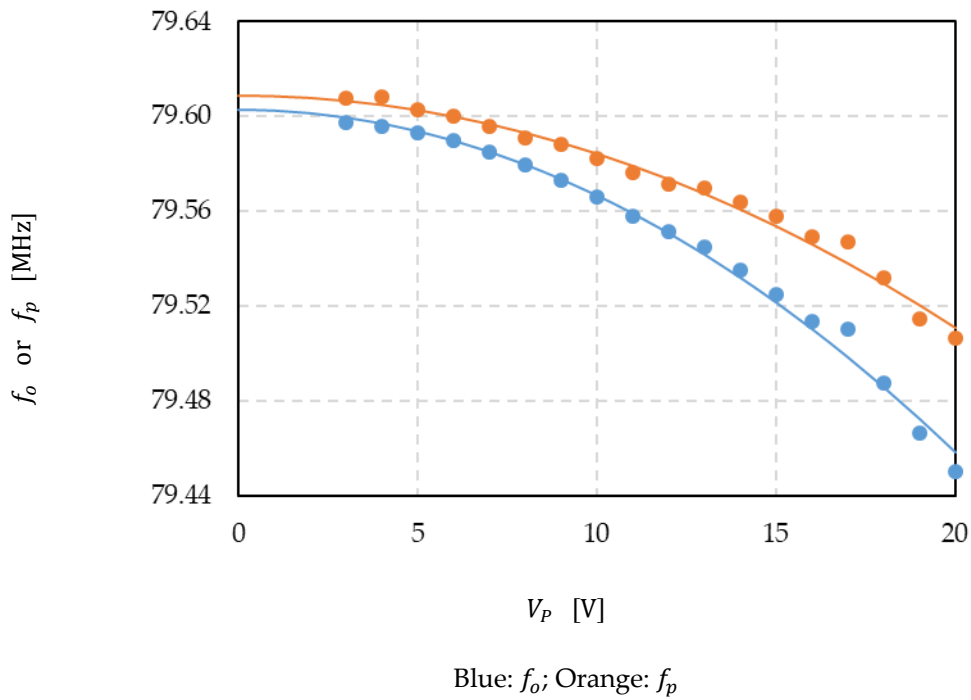
Blue: f_o; Orange: f_p

Figure 2.23: Resonance and parallel frequencies versus DC bias voltage

Blue: C_x/C_e; Orange: C_x/C_o

Figure 2.25: C_x/C_e and C_x/C_o versus DC bias voltage

2.6 Conclusions

In conclusion, it is evident that an asymmetric hollow disk design can boost C_x/C_o. An 80 MHz asymmetric radial contour hollow disk achieves $C_x/C_o = 0.142\%$ and $C_x/C_e = 0.358\%$ with an 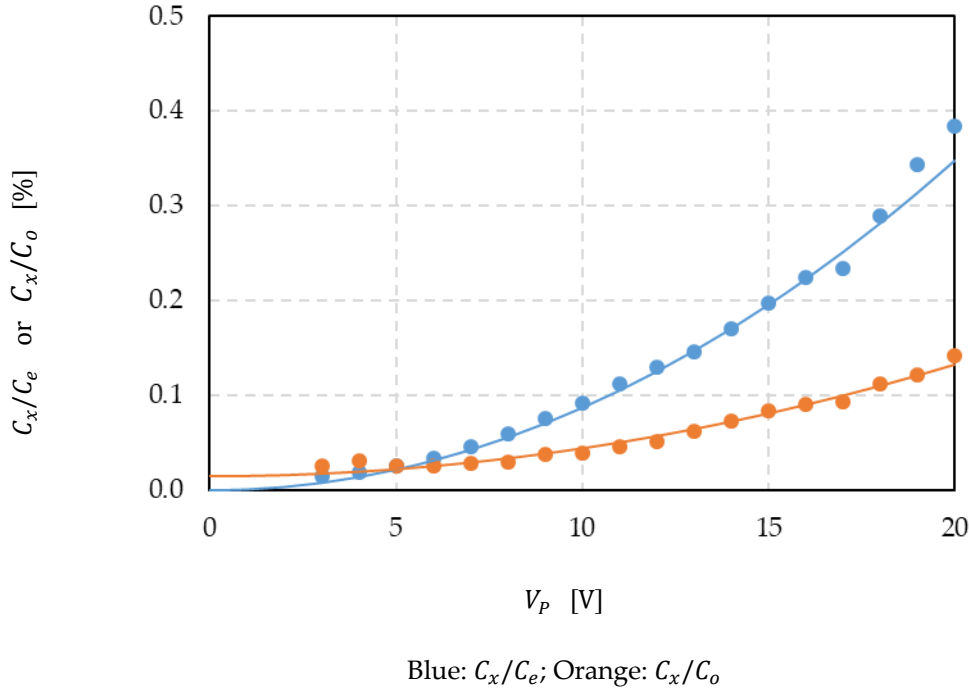148 nm electrode-to-resonator gap and a 20 V DC bias, which is much higher than $C_x/C_o = 0.015\%$ of a similar frequency solid disk. On the one hand, there is less dynamic mass, which is inversely proportional to C_x/C_o, because the disk is hollow. On the other hand, FEA proves that the sidewall vibrates in the radial cantilever mode in the radial direction, and its vertical vibration is negligible. Its radial vibration introduces a nonlinear coefficient (λ) in electromechanical coupling ratio (η_e). Since λ is larger than 1, the sidewall can boost C_x/C_o even higher by boosting η_e.

The inner disk vibrates in the radial contour mode in the radial direction, but it also vibrates transversely, which introduces an extra dynamic mass moving in the vertical direction. Since C_x/C_o is inversely proportional to mass, the nonideality lowers C_x/C_o, but only by a very small amount. In addition, the hollow structure reduces the nominal frequency. These nonidealities will become more critical if the disk is hollower.

Sections 2.1 and 2.5 conduct a detailed analysis of the negative capacitance equivalent circuit in [9]. The parallel frequency (f_p) equals the nominal frequency (f_{nom}) only if $C_e = C_o$. However, this assumption is not accurate for the 80 MHz asymmetric hollow disk because its f_p is dependent on DC bias. As a result, C_e of this hollow disk is only $0.322C_o$.

CHAPTER 3

SYMMETRIC HOLLOW DISK

3.1 Symmetric Hollow Disk Design

Asymmetric hollow disks tend to vibrate both radially and transversely. The transverse vibration of the inner disk introduces an extra dynamic mass moving in the vertical direction in the mechanical domain. This mass reduces the motional-to-static capacitive ratio (C_x/C_o). A symmetric hollow disk can eliminate this nonideality. Figure 3.2 schematically shows a symmetric radial contour hollow disk with a fully surrounded electrode. In this symmetric structure, a sidewall ring protrudes in both upwards and downwards directions along the inner disk edges. The hollow disk is more symmetric in the vertical direction.

(a)   (b)
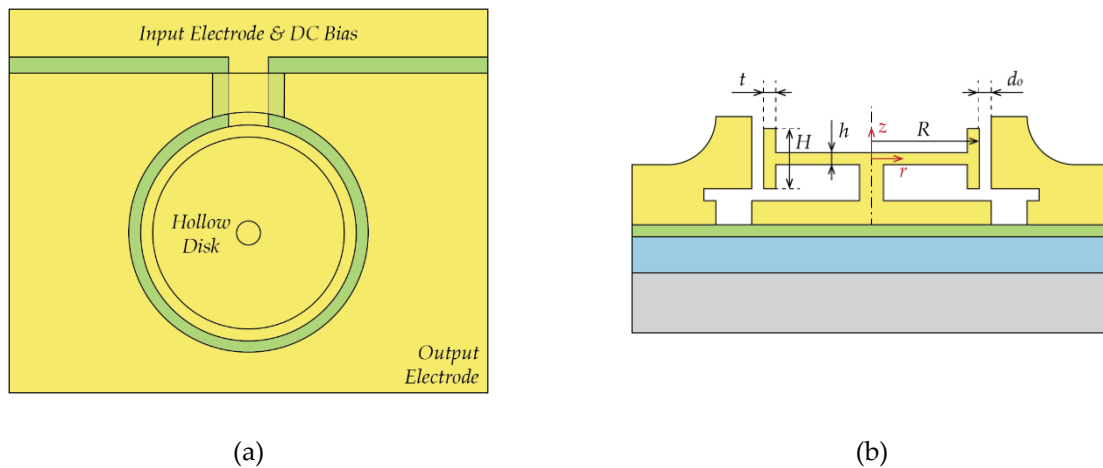
Figure 3.1: Schematic showing a symmetric hollow disk with a fully surrounded electrode
and variables used in derivation: (a) top view and (b) cross-section view

Figure 3.2 presents simulated mode shapes of a symmetric hollow disk and a solid disk for comparison. The symmetric hollow disk vibrates in the radial contour mode as the solid disk. There is no transverse vibration in the inner disk. Additionally, both sidewalls vibrate uniformly.
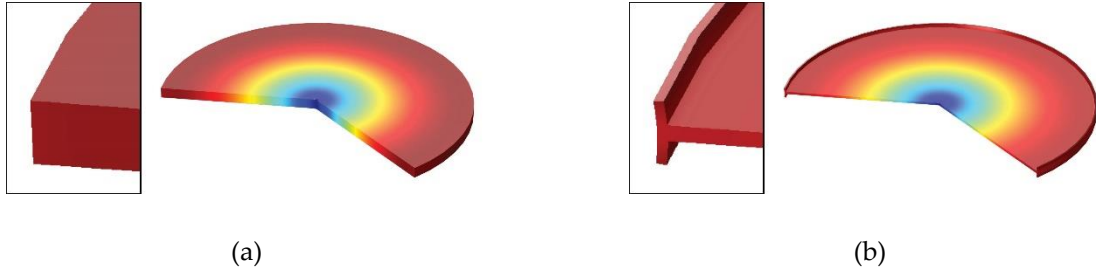
Figure 3.2: Radial contour mode shapes of (a) a solid disk and (b) a symmetric hollow disk

Equivalent circuits in Figure 2.2 can model this symmetric hollow disk as well. In addition, the ideal radial contour function in [9] can derive all equivalent circuit variables by

$$R_{mode}(r) = J_1(\varphi r), \quad \varphi = \sqrt{\frac{(2\pi f_{nom})^2 \rho}{\frac{E}{1-v^2}}} \tag{3.1}$$

where J_1 is the Bessel function, φ is a constant that depends on the nominal frequency (f_{nom}), density (ρ), Young's modulus (E), and Poisson's ratio (v). Based on the derivation in [9], the only difference is that the total motion mass (m_m) or mechanical inductance (l_x) is the sum of the disk and the sidewall,

$$l_x = m_m(R) = \frac{\iiint [R_{mode}(r)]^2 dm}{[R_{mode}(r_{ref})]^2}$$
$$= \frac{2\pi\rho \left\{ h \int_0^{R-t} [R_{mode}(r)]^2 r dr + H \int_{R-t}^{R} [R_{mode}(r)]^2 r dr \right\}}{[R_{mode}(R)]^2} \tag{3.2}$$

Table 3.1 summarizes detailed design and equivalent circuit variables of a 128 MHz asymmetric hollow disk. All geometric dimensions of the structure (i.e., R, H, h, t, and d_o) are from measurements during fabrication. It is a reasonable assumption for a hollow disk that the DC bias voltage (V_P) is 10 V and the quality factor (Q) is 5000. Equations (2.2) -- (2.11) give all equivalent circuit variables if $C_e = C_o$. The table shows a 128 MHz solid radial contour disk as well for comparison. The dynamic mass of the hollow disk is only 27% of the original in the solid disk. As a result, the hollow disk can boost C_x/C_o by approximately four times and lower the motional resistance (R_x) by 73%.

Unfortunately, post-fabrication stress gradients rendered testable only a large-stemmed symmetric hollow disk. Section 3.2 will discuss this type of hollow disk with its nonidealities.

Table 3.1: Summary of detail design and equivalent circuit variables of the 128 MHz symmetric hollow disk and an 128 MHz solid disk

	Parameters	Solid Disk	Hollow Disk	Units
Design Variables	Disk Radius (outer), R	20.6	20.6	μm
	Total Height, H	2.4	2.4	μm
	Inner Disk Thickness, h	--	500	nm
	Sidewall Thickness, t	--	600	nm
	Electrode-to-Resonator Gap, d_o	50	50	nm
	DC Bias Voltage, V_P	10	10	V
	Quality Factor, Q	5000	5000	--
	Nominal Frequency, f_{nom}	128.202	128.202	MHz
	Resonance Frequency, f_o	128.163	128.057	MHz
Equivalent Circuit Variables	Mech. Inductance (mass), l_x	5.616	1.506	pH
	Mech. Capacitance (1/stiffness), c_x	0.274	1.023	μF
	Mech. Resistance (damping), r_x	0.905	0.243	μΩ
	Static Overlap Capacitance, C_o	55.010	55.010	fF
	Electromechanical Coupling Ratio, η_e	11.002	11.002	μC/m
	Motional Inductance, L_x	0.046	0.012	H
	Motional Capacitance, C_x	0.033	0.124	fF
	Motional Resistance, R_x	7.475	2.005	kΩ
	C_x-to-C_o Capacitive Ratio, C_x/C_o	0.060	0.225	%

3.2 Symmetric Hollow Disk Design with a Large Stem

Figure 3.3 schematically shows a symmetric hollow disk with a large stem and a fully surrounded electrode.

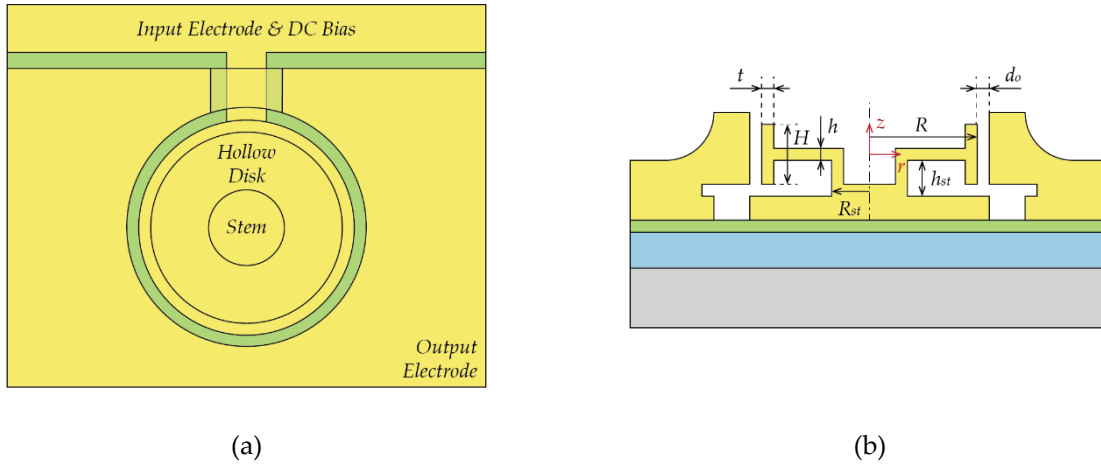(a)   (b)

Figure 3.3: Schematic showing a symmetric hollow disk with a large stem and variables used in derivation: (a) top view and (b) cross-section view

Table 3.2 summarizes detailed design and equivalent circuit variables of a 98 MHz symmetric hollow disk with a large stem whose radius is 8 µm. Figure 3.4 shows its simulated mode shape. Like the asymmetric hollow disk, the inner disk vibrates not only radially but also transversely.

To analyze how the hollow disk vibrates in the radial and vertical directions respectively. Figure 3.5 presents simulated radial and vertical mode shape functions. It is evident that there is undulation in the vertical mode shape function of the inner disk, although it still vibrates radially. Thus, follow the same procedure as Section 2.1 to analyze the device.

Figure 3.6 shows the radial mode shape function of the sidewall, which proves that the displacement function along the sidewall is linear. In other words, unlike the asymmetric hollow disk, the symmetric circular sidewall does not vibrate by itself but driven by the inner disk.

Like the asymmetric hollow disk, the rest design variables in Table 3.2 (i.e., V_P, Q, f_{nom}, and f_o) are from the device measurement in Section 3.4. Volume or surface integrations can extract all equivalent circuit variables based on the simulated mode shape function directly.

Table 3.2: Summary of design and two-direction equivalent circuit variables of the 98 MHz symmetric hollow disk with a large stem

	Parameters	Asymmetric Hollow Disk		Units
Design Variables	Disk Radius (outer), R	20.6		µm
	Total Height, H	2.4		µm
	Inner Disk Thickness, h	500		nm
	Sidewall Thickness, t	600		nm
	Electrode-to-Resonator Gap, d_o	50		nm
	Outer Stem Radius, R_{st}	8		µm
	DC Bias Voltage, V_P	7		V
	Quality Factor, Q	1500		--
	Nominal Frequency, f_{nom}	98.048		MHz
	Resonance Frequency, f_o	97.837		MHz
Equivalent Circuit Variables	Mech. Inductance (mass), l_x	1.530		pH
	Mech. Capacitance (1/stiffness), c_x	1.723		µF
	Mech. Resistance (damping), r_x	0.628		µΩ
	Static Overlap Capacitance, C_o	70.364		fF
	Electromechanical Coupling Ratio, η_e	8.857		µC/m
	Motional Inductance, L_x	0.020		H
	Motional Capacitance, C_x	0.135		fF
	Motional Resistance, R_x	8.009		kΩ
	Electrical Stiffness Equiv. Cap., $-C_e$	-31.117		fF
	Capacitive Ratio	$C_x/C_e = 0.430\%$	$C_x/C_o = 0.261\%$	--

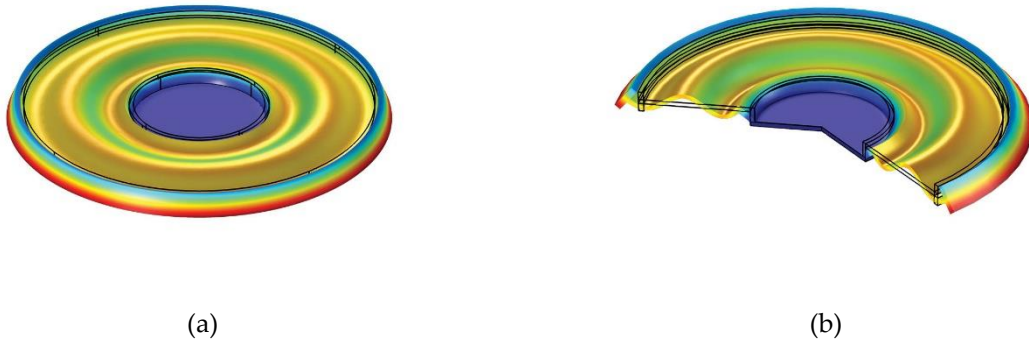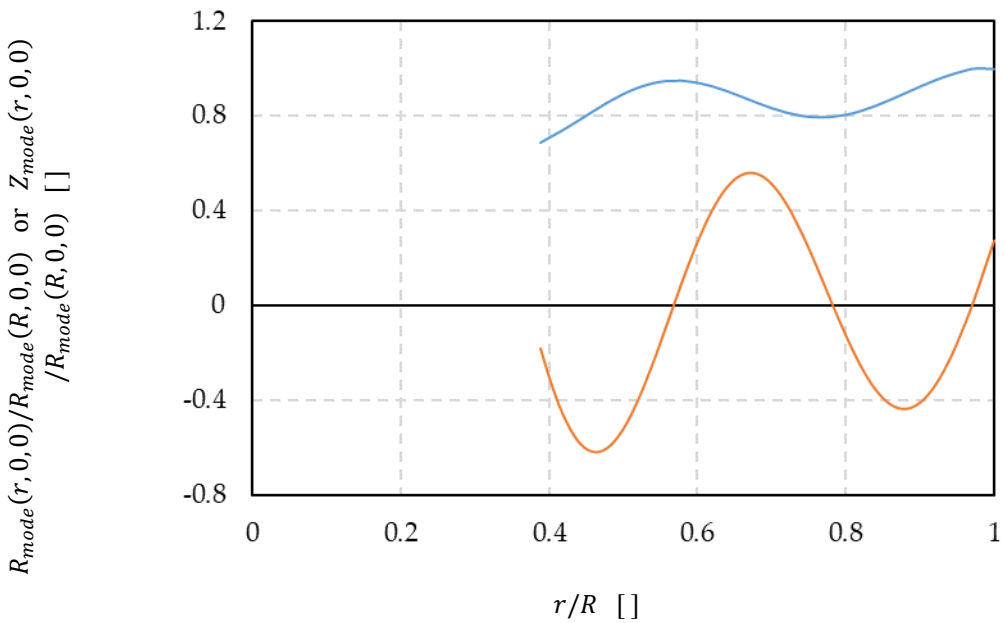(a)   (b)

Figure 3.4: Mode shape of the designed 98 MHz symmetric hollow disk with a large stem: (a) 3D FEA; (b) 2D FEA

Blue: radial mode shape function; Orange: vertical mode shape function

Figure 3.5: Simulated normalized radial and vertical mode shape functions of the inner disk of the hollow disk
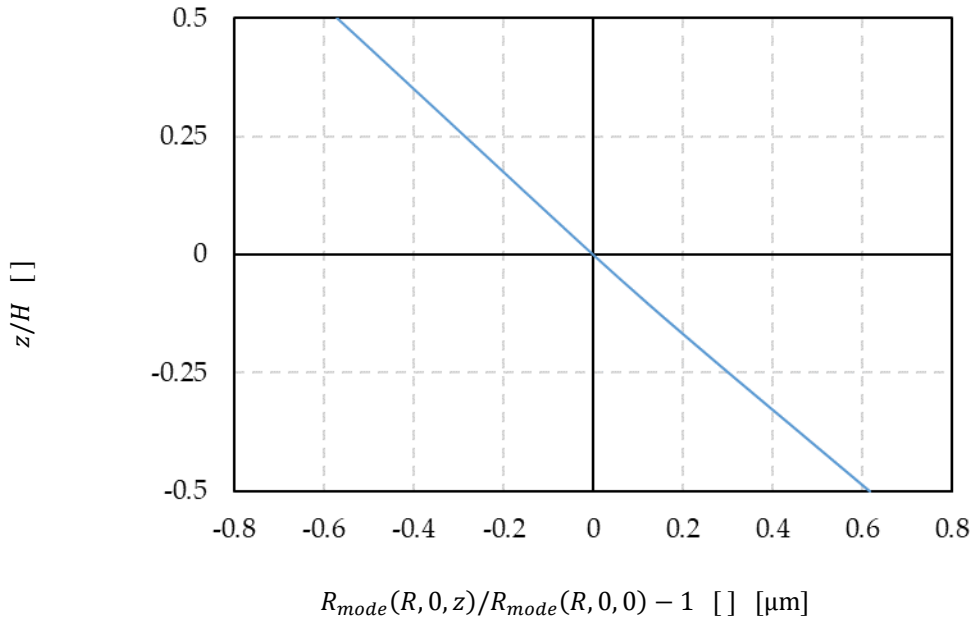
Figure 3.6: Simulated normalized radial mode shape function of the sidewall of the hollow disk

3.3 Fabrication Process

Figure 3.7 and Table 3.3 summarize the fabrication process yielding symmetric hollow disks. This process flow includes an extra step of timed etch (i.e., Step b-3), but industrial applications usually avoid timed etch because it is hard to control the uniformity of the etch rate throughout the wafer and from wafer to wafer. An optimized process might add a thin layer as etch stop in the thick silicon dioxide in the future.

Figure 3.8 (a) presents a scanning electron micrograph (SEM) of a fabricated symmetric hollow disk with a fully surrounded electrode and a small stem, but the resonator shorts with the electrode after release due to a large stress gradient. Figure 3.8 (b) shows the cross-section view of a dummy device after Step c-1, which shows the symmetric hollow structure.

After release, the profile measurement of the hollow disk in Figure 3.8 (a) explains why the device shorts out. The disk bends down and the vertical deflection of the disk's edge is $\Delta = 0.11$ µm. Since the radius of the disk is $R = 24$ µm, the stress gradient in the inner disk is

$$\Gamma = \frac{2\Delta}{R^2} = 3.85 \times 10^{-4} \ \mu m^{-1} \tag{3.3}$$

This stress gradient is large enough to short a 50 nm gap, especially in large structures.

(a)

(b)

(c)

(d)

(e)
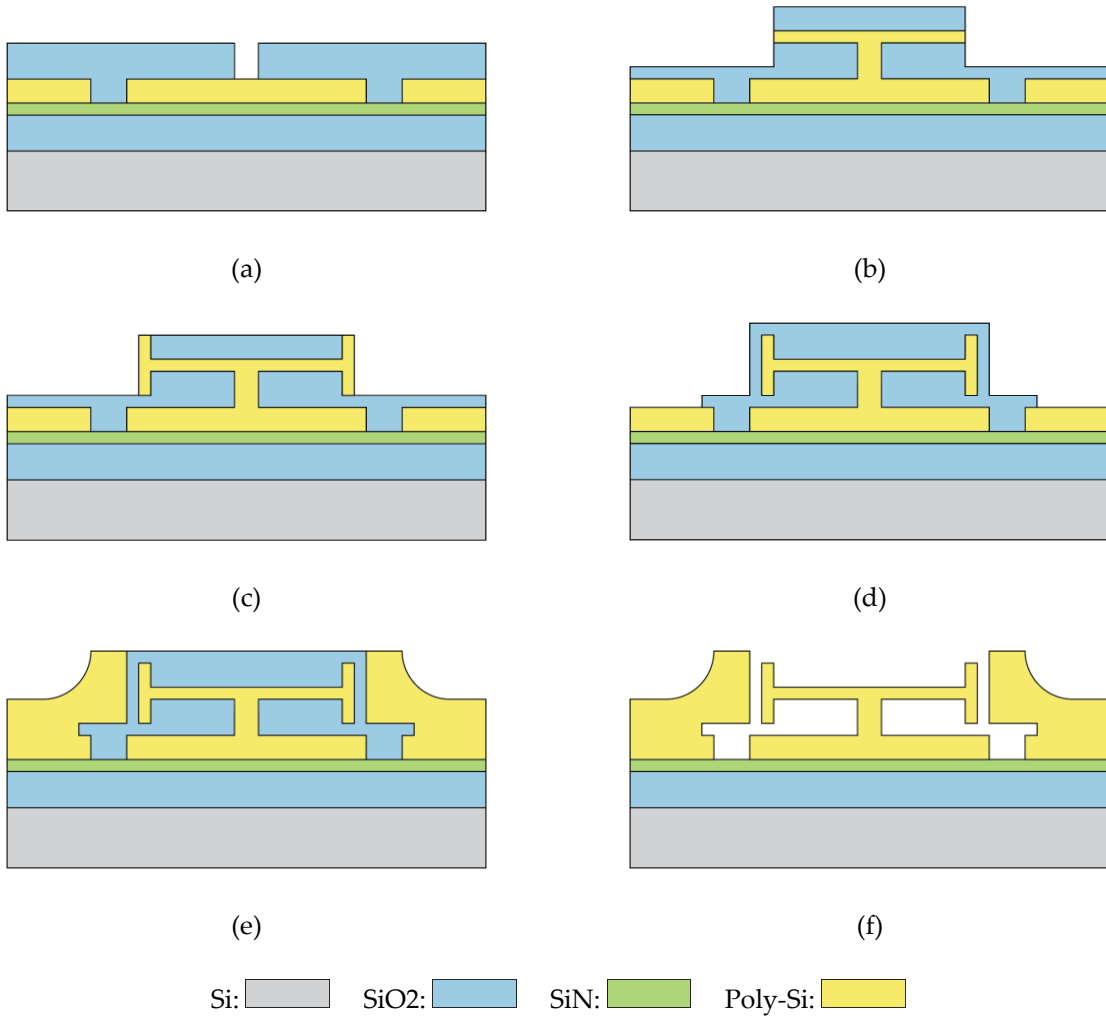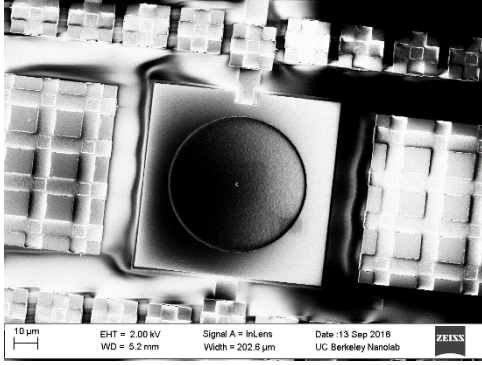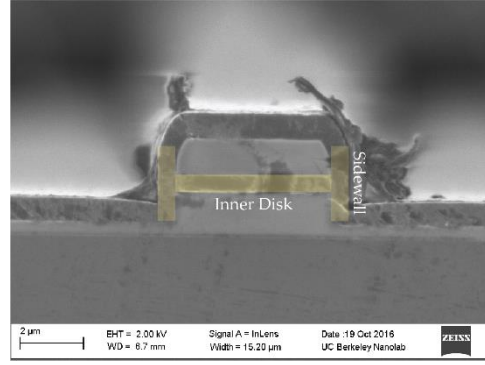
(f)

Si: ⬜ SiO2: ⬜ SiN: ⬜ Poly-Si: ⬜

Figure 3.7: Fabrication process yielding symmetric hollow disks with more detailed information shown in Table 3.3

Table 3.3: Detailed fabrication process yielding symmetric hollow disks

Figure	Step	Fabrication	Details	Tools
(a)	a-1	Deposition	LPCVD 2 μm LTO	tyster 11 & 2
	a-2	Deposition	LPCVD 500 nm LSN	tyster 9
	a-3	Deposition	LPCVD 1 μm LTO	tyster 11 & 2
	a-4 (m1)	Patterning	RIE SiO$_2$ (by Mask #1, m1)	asml 300 & sts-oxide
	a-5	Deposition	LPCVD 1.5 μm Si (doped)	tyster 10 & 6
	a-6	CMP	CMP Si (stopped on SiO$_2$)	cmp
	a-7	Deposition	LPCVD 1.5 μm LTO	tyster 12 & 3
	a- 8 (m2)	Patterning	RIE SiO$_2$ (by Mask #2, m2)	asml 300 & sts-oxide
(b)	b-1	Deposition	LPCVD 500 nm Si (doped)	tyster 16 & 3
	b-2	Deposition	LPCVD 2.2 μm LTO	tyster 12 & 4
	b-3 (m3)	Patterning	RIE SiO$_2$, Si and SiO$_2$ (timed etch) (by Mask #3, m3)	asml 300 & sts-oxide & sts2
(c)	c-1	Deposition	LPCVD 600 nm Si (doped)	tyster 16 & 3
	c-2	Etching	Blank RIE Si (without a mask)	sts2
(d)	d-1	Deposition	LPCVD 50 nm HTO	tyster 17
	d-2 (m4)	Patterning	RIE SiO$_2$ (by Mask #4, m4)	asml 300 & sts-oxide
(e)	e-1	Deposition	LPCVD 3 μm Si (doped)	tyster 16 & 6
	e-2	CMP	CMP Si (stopped on SiO$_2$)	cmp
	e-3 (m5)	Patterning	RIE Si (by Mask #5, m5)	asml 300 & sts2
(f)	f-1	Release	HF Release	msink 18

<div style="text-align:center">(a)　　　　　　　　　　　　　　　　(b)</div>

Figure 3.8: SEMs of (a) a fabricated hollow disk with a fully surrounded electrode and (b) the cross-section view of a dummy device after Step c-1

3.4 Measurement Results

Follow the same procedure as Section 2.5, this section will discuss measurement of the fabricated 98 MHz symmetric hollow disk with a large stem and characterization of the model in Section 2.2. Its quality factor is only 1500 due to the anchor loss. Figure 3.9 presents measured frequency responses with various DC bias voltages. Figure 3.10 presents measured and modeled resonance and parallel frequencies versus DC bias (V_P). Both are parabolically dependent on V_P, so linear regression of frequencies on V_P^2 yields

$$f_o = f_{nom} - \varphi_o V_P^2 = 98.048 \times 10^6 - 4295 V_P^2 \tag{3.4}$$

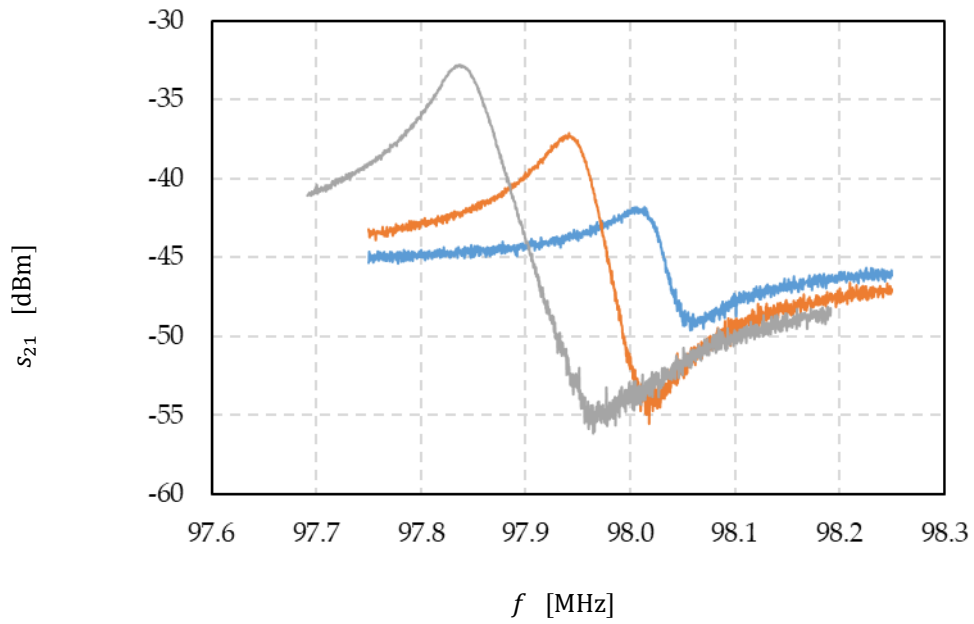$$f_p = f_{nom} - \varphi_p V_P^2 = 98.082 \times 10^6 - 2396 V_P^2 \tag{3.5}$$

which are the blue and orange lines in Figure 3.10. Both lines yield approximately the same nominal frequency. Taking the ratio of two slopes yields

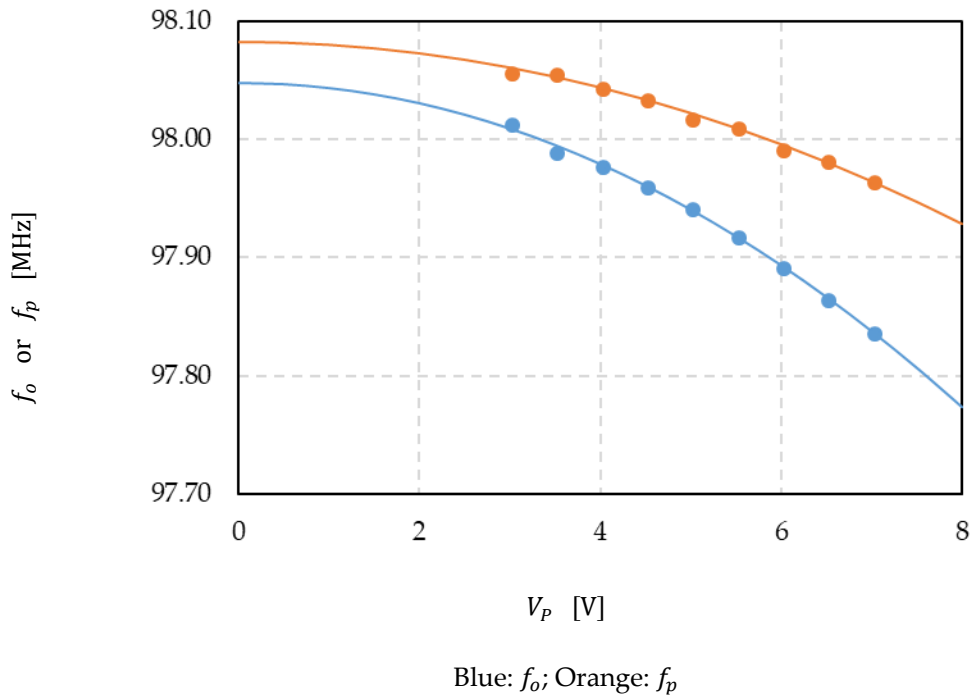$$\kappa = \frac{\varphi_o}{\varphi_p} = 1.793 \tag{3.6}$$

Substitution of Equation (3.6) in (2.50) yields

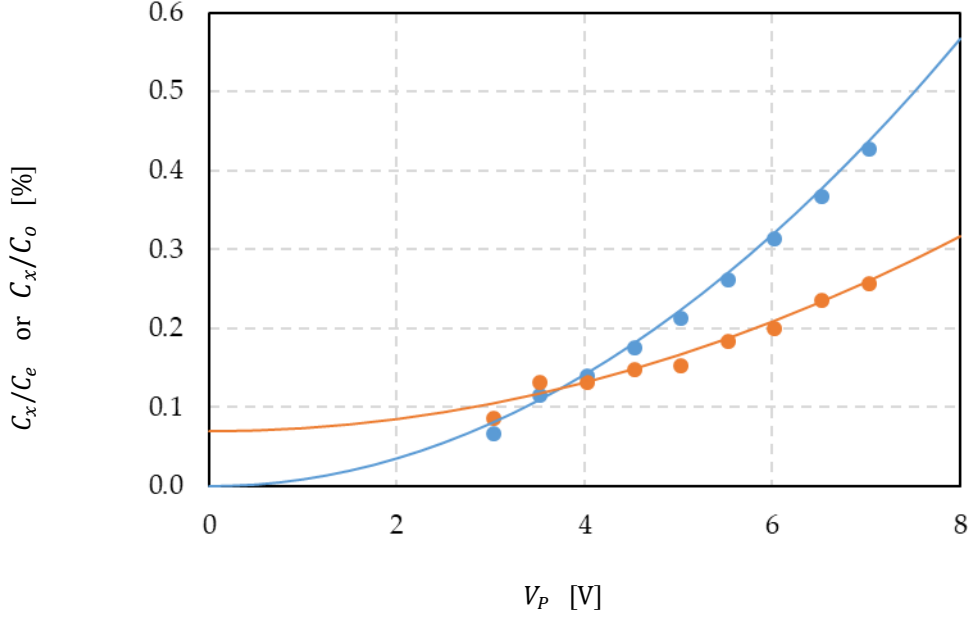$$C_e = \frac{\kappa - 1}{\kappa} C_o = 0.442 C_o \tag{3.7}$$

Gray: $V_P = 7$ V; Orange: $V_P = 5$ V; Blue: $V_P = 3$ V

Figure 3.9: Frequency responses of the 98 MHz hollow disk with various DC bias voltages

Blue: f_o; Orange: f_p

Figure 3.10: Resonance and parallel frequencies versus DC bias voltage

Blue: C_x/C_e; Orange: C_x/C_o

Figure 3.11: C_x/C_e and C_x/C_o versus DC bias voltage

Thus, unlike the equivalent circuit in [9], C_e does not equal C_o because f_p is voltage dependent. C_e of this hollow disk is 31.117 fF and C_o is 70.364 fF.

According to Equations (2.11) and (2.21), Figure 3.11 presents measured and modeled C_x/C_e and C_x/C_o. As a result, C_x/C_e of this hollow disk is 0.430% and C_x/C_o is 0.261% at $V_P = 7$ V.

3.5 Conclusions

In conclusion, a symmetric hollow disk can not only boost C_x/C_o but also eliminate the transverse vibration nonideality. A designed 128 MHz symmetric radial contour hollow disk can achieve $C_x/C_o = 0.225\%$, with a 50 nm electrode-to-resonator gap and a 10 V DC bias, which is much higher than $C_x/C_o = 0.060\%$ of a similar frequency solid disk. Unfortunately, post-fabrication stress gradients rendered testable only a few large-stemmed hollow disks.

A 98 MHz symmetric hollow disk with an 8 μm radius stem survived after release, but its mode shape becomes nonideal and the quality factor is lower. Like the asymmetric hollow disk,

the inner disk vibrates both transversely and radially. Unlike the asymmetric one, the sidewall does not vibrate by itself but driven by the inner disk.

The 98 MHz hollow disk achieves $C_x/C_o = 0.261\%$ and $C_x/C_e = 0.430\%$ with a 50 nm electrode-to-resonator gap and a 7 V DC bias, and they are higher than solid disks. The same phenomenon of $C_e \neq C_o$ happens in this device again, in which C_e is only $0.442C_o$. This is the reason the parallel frequency (f_p) is parabolically dependent on DC bias.

CHAPTER 4

CONCLUSIONS

4.1 Achievements

This thesis successfully introduces a new hollow disk method to boost the electromechanical coupling gauged by motional-to-static capacitive ratio (C_x/C_o), which can be widely used in applications for wireless communication. Particularly, this work achieves the following results:

1. Compared to solid disks, both asymmetric and symmetric hollow disks can boost C_x/C_o. Table 4.1 summarizes three successful designs in this thesis.

Table 4.1: Summary of asymmetric and symmetric hollow disks in this thesis and solid disks for comparison

Disk Types	f_o	d_o	V_P	C_x/C_e	C_x/C_o
Asymmetric	79.450 MHz	148 nm	20 V	0.384%	0.142%
Solid	81.631 MHz			0.015%	0.015%
Symmetric*	128.057 MHz	50 nm	10 V	0.225%	0.225%
Solid	128.163 MHz			0.060%	0.060%
Symmetric w/ Large Stem	97.837 MHz	50 nm	7 V	0.430%	0.261%

* Due to the large stress gradient in the polysilicon structural layer of the inner disk, none of this type of hollow disks survives after release. The performance of this device is from modeling.

2. C_x/C_o is inversely proportional to dynamic mass. Hollow disks have less mass moving during vibration and this is one of the reasons C_x/C_o can be boosted. Unlike symmetric hollow disks, the circular sidewall of an asymmetric hollow disk vibrates by itself in the radial cantilever mode. This radial vibration introduces a nonlinear coefficient (λ) in

46

electromechanical coupling ratio (η_e). Since λ is larger than 1, the sidewall can boost C_x/C_o even higher by boosting η_e.

3. Hollow disks tend to vibrate not only radially but also transversely unless they are perfectly symmetric in the vertical direction (i.e., symmetric hollow disks with a small stem). The vertical vibration introduces an extra dynamic mass moving in the vertical direction. Since C_x/C_o is inversely proportional to the total mass, this nonideality lowers C_x/C_o, but only by a very small amount. In addition, the hollow structure reduces the nominal frequency. These nonidealities become more critical when the disk is hollower.

4. Both chapters conduct a detailed analysis of the negative capacitance equivalent circuit in [9]. The parallel frequency (f_p) equals the nominal frequency (f_{nom}) only if $C_e = C_o$. However, this assumption is not correct for some hollow disks because its f_p is instead dependent on DC bias. As a result, C_x/C_e is higher than C_x/C_o as shown in Table 4.1.

4.2 Future Research Directions

This thesis successfully demonstrates the approach of hollow disk C_x/C_o boosting for the first time, so more investigation and optimization of the design are necessary for the future. In particular, researchers can apply more research efforts in the following directions:

1. Lower the stress gradient in the polysilicon structural layer of the inner disk by optimizing deposition and annealing processes, which will prevent the disk bending down.

2. Improve the roughness of the sidewall by optimizing deposition and etching processes, which will allow shrinking the gap and rising the DC bias even further.

3. Create a method to measure the transverse vibration by putting more electrodes underneath the disk, which will allow proving the equivalent circuit model.

REFERENCES

[1].   C. Auth et al., "A 10nm high performance and low-power CMOS technology featuring 3rd generation FinFET transistors, Self-Aligned Quad Patterning, contact over active gate and cobalt local interconnects," 2017 IEEE International Electron Devices Meeting (IEDM), San Francisco, CA, 2017, pp. 29.1.1-29.1.4. DOI: 10.1109/IEDM.2017.8268472

[2].   M. A. Abdelmoneum, M. U. Demirci and C. T. C. Nguyen, "Stemless wine-glass-mode disk micromechanical resonators," The Sixteenth Annual International Conference on Micro Electro Mechanical Systems, 2003. MEMS-03 Kyoto. IEEE, 2003, pp. 698-701. DOI: 10.1109/MEMSYS.2003.1189845

[3].   T. L. Naing et al., "2.97-GHz CVD diamond ring resonator with Q >40,000," 2012 IEEE International Frequency Control Symposium Proceedings, Baltimore, MD, 2012, pp. 1-6. DOI: 10.1109/FCS.2012.6243723

[4].   M. Akgul and C. T. C. Nguyen, "A passband-corrected high rejection channel-select micromechanical disk filter," 2014 IEEE International Frequency Control Symposium (FCS), Taipei, 2014, pp. 1-6. DOI: 10.1109/FCS.2014.6860009

[5].   T. L. Naing, T. O. Rocheleau, E. Alon and C. T. C. Nguyen, "A 78-microwatt GSM phase noise-compliant pierce oscillator referenced to a 61-MHz wine-glass disk resonator," 2013 Joint European Frequency and Time Forum & International Frequency Control Symposium (EFTF/IFC), Prague, 2013, pp. 562-565. DOI: 10.1109/EFTF-IFC.2013.6702305

[6].   R. Liu, J. N. Nilchi and C. T. C. Nguyen, "CW-powered squegging micromechanical clock generator," 2017 IEEE 30th International Conference on Micro Electro Mechanical Systems (MEMS), Las Vegas, NV, 2017, pp. 905-908. DOI: 10.1109/MEMSYS.2017.7863555

[7].   J. N. Nilchi, R. Liu and C. T. C. Nguyen, "High Cx/Co 13nm-capacitive-gap transduced disk resonator," 2017 IEEE 30th International Conference on Micro Electro Mechanical Systems (MEMS), Las Vegas, NV, 2017, pp. 924-927. DOI: 10.1109/MEMSYS.2017.7863560

[8].   J. Naghsh Nilchi, R. Liu and C. T. C. Nguyen, "7th order sharp-roll-off bridged micromechanical filter," 2015 Transducers - 2015 18th International Conference on Solid-State Sensors, Actuators and Microsystems (TRANSDUCERS), Anchorage, AK, 2015, pp. 137-140. DOI: 10.1109/TRANSDUCERS.2015.7180880

[9].   M. Akgul, L. Wu, Z. Ren and C. T. C. Nguyen, "A negative-capacitance equivalent circuit model for parallel-plate capacitive-gap-transduced micromechanical resonators," in IEEE

Transactions on Ultrasonics, Ferroelectrics, and Frequency Control, vol. 61, no. 5, pp. 849-869, May 2014. DOI: 10.1109/TUFFC.2014.2976

[10]. M. Akgul et al. "Capacitively transduced micromechanical resonators with simultaneous low motional resistance and Q>70,000" in Hilton-Head, 2010

[11]. C. Auth et al., "A 10nm high performance and low-power CMOS technology featuring 3rd generation FinFET transistors, Self-Aligned Quad Patterning, contact over active gate and cobalt local interconnects," 2017 IEEE International Electron Devices Meeting (IEDM), San Francisco, CA, 2017, pp. 29.1.1-29.1.4. DOI: 10.1109/IEDM.2017.8268472

[12]. L. Wu, M. Akgul, Z. Ren, Y. Lin, W. C. Li and C. T. C. Nguyen, "Hollow stems for higher micromechanical disk resonator quality factor," 2011 IEEE International Ultrasonics Symposium, Orlando, FL, 2011, pp. 1964-1967. DOI: 10.1109/ULTSYM.2011.6293678